

# The origin of the UV excess in powerful radio galaxies: spectroscopy and polarimetry of a complete sample of intermediate redshift radio galaxies

C. Tadhunter<sup>1</sup>, R. Dickson<sup>2</sup>, R. Morganti<sup>3</sup>, T.G. Robinson<sup>1</sup>, K. Wills<sup>1</sup>,  
M. Villar-Martin<sup>4</sup>, M. Hughes<sup>4</sup>

<sup>1</sup>*Department of Physics and Astronomy, University of Sheffield, Hounsfield Road, Sheffield, S3 7RH, UK*

<sup>2</sup>*Jodrell Bank Observatory, University of Manchester, Macclesfield, Cheshire, SK11 9DL.*

<sup>3</sup>*Netherlands Foundation for Research in Astronomy, Postbus 2, 7990 AA Dwingeloo, The Netherlands*

<sup>4</sup>*Division of Physical Sciences, University of Hertfordshire, Herts*

## ABSTRACT

We present spectroscopic and polarimetric observations of a complete, optically unbiased sample of 2Jy radio galaxies at intermediate redshifts ( $0.15 < z < 0.7$ ). These data — which cover the nuclear regions of the target galaxies — allow us to quantify for the first time the various components that contribute to the UV excess in the population of powerful, intermediate redshift radio galaxies. We find that, contrary to the results of previous surveys — which have tended to be biased towards the most luminous and spectacular objects in any redshift range — the contribution of scattered quasar light to the UV excess is relatively minor in most of the objects in our sample. Only 7 objects (32% of the complete sample) show significant polarization in the rest-frame UV, and none of the objects in our sample is polarized in the near-UV at the  $P > 10\%$  level. Careful measurement and modelling of our spectra have allowed us to quantify the contributions of other components to the UV excess. We show that nebular continuum (present in all objects at the 3 — 40% level), direct AGN light (significant in 40% of objects), and young stellar populations (significant in 15 — 50% of objects) all make important contributions to the UV continuum in the population of powerful radio galaxies. These results serve to emphasise the multi-component nature of the UV continuum in radio galaxies. The results also point to an interesting link between the optical/UV and far-IR properties of our sample objects, in the sense that the objects with the clearest evidence for optical/UV starburst activity are also the most luminous at far-IR wavelengths. This supports the idea that the cooler dust components in radio galaxies are heated by starbursts rather than by AGN.

**Key words:** galaxies:active – galaxies:individual – galaxies:emission lines – quasars:general

## 1 INTRODUCTION

Given the large look back times encompassed by the most distant radio sources, one motivation for studying such objects is their potential use as probes of the formation and evolution of giant early-type galaxies in the early universe. However, all studies aimed at using radio galaxies in this way have to face the problem of distinguishing the effects of the AGN and radio jet activity from genuine signs of galaxy evolution. This problem is particularly acute in the case of studies of the continuum properties. Compared with normal early-type galaxies, powerful radio galaxies can show continuum excesses at both optical/UV (e.g. Lilly & Longair 1984, Smith & Heckman 1989) and far-IR/sub-mm wavelengths

(Golombek et al. 1988, Heckman et al. 1994, Archibald et al. 2001). Therefore, a key issue for these objects is whether these continuum excesses are a consequence of recent star formation which may be linked to evolutionary processes in the early-type host galaxies or, given that these objects contain powerful AGN and radio jets, a direct consequence of the activity.

The presence of a UV excess in the continua of radio galaxies was first demonstrated by the photometric observations of samples of high redshift ( $z > 0.5$ ) radio galaxies in the early 1980's. These observations showed evidence for bluer optical-IR colours than expected for non-evolving or passively evolving elliptical galaxies (e.g. Lilly & Longair

1984). Initially, the UV excess was interpreted in terms of bursts of star formation, possibly linked to the evolution of the host galaxies. This interpretation is attractive in the light of morphological studies which show evidence for recent mergers in a large fraction of powerful radio galaxies at low redshifts (Heckman et al. 1986); and merger-induced star formation has been suggested as a possible triggering mechanism (Smith & Heckman 1989). However, given the degree of nuclear and extranuclear activity likely to be present in most powerful radio galaxies, some caution is required in deducing starburst properties purely on the basis of broadband photometric measurements.

Recognising the potential AGN contribution, an alternative explanation for the UV excess was stimulated by the development of the anisotropy-based unified schemes in the late 1980's (e.g. Barthel 1989). In the frame of such schemes the UV excesses can be explained in terms of light scattered from broad radiation cones of the hidden quasar nuclei (Tadhunter et al. 1988, Fabian 1989). Early polarimetric attempts to test this model proved successful in the sense that they showed the high degrees of linear polarization characteristic of anisotropic scattering in the UV continua of several high redshift radio galaxies (e.g. Tadhunter et al. 1992, Cimatti et al. 1993, Vernet et al. 2001). However, while these observations demonstrate that scattered quasar light is an important component of the UV continuum in *some* sources, they do not establish the significance of the scattered component in the general population of powerful radio galaxies. Because polarimetric observations of faint objects are difficult, previous studies have tended to be biased towards the brightest, most spectacular objects in a given redshift range. There are also redshift-dependent biases which arise because optical (mostly V-band) observations sample the rest-frame UV in the high redshift objects — with minimal dilution by the old stellar populations of the host galaxies — but sample the rest-frame optical in the low redshift objects — with substantial dilution by the old stellar populations. The importance of this observational selection effect is emphasised by multi-wavelength polarimetric observations of individual sources which show a sharp decline in the measured polarization between the UV and the optical (Tadhunter et al. 1996, Ogle et al. 1997, Tran et al. 1998).

In addition to the scattered component, detailed observations over the last decade have revealed the presence of two further activity-related components which can contribute to the UV excess. These are: the nebular continuum emitted by the extended emission line nebulae (Dickson et al. 1995); and direct AGN light emitted by weak, or partially extinguished, quasars in the nuclei of the galaxies (Shaw et al. 1995). The nebular continuum is likely to be particularly significant in regions where the emission lines have large equivalent widths, including the extended emission line nebulae around powerful radio galaxies. In contrast, the direct AGN component will only be important in the nuclear regions of the sources.

Most recently, events have turned full circle with the spectroscopic detection of young stellar populations in at least some powerful radio galaxies (e.g. Tadhunter et al. 1996, Melnick et al. 1997). The detection of this component is consistent with the early interpretation of the UV excess in terms of starbursts associated with the evolution of the host galaxies (Lilly & Longair 1984). Unfortunately, apart

from cases in which it dominates the optical continuum (e.g. Miller 1981), the starburst component is notoriously difficult to detect at optical wavelengths. Its presence can be masked by the light of the old stellar populations in the bulges of the host galaxies, by the various activity-related continuum components noted above, and by emission lines which can contaminate the absorption features characteristic of young stars. This is illustrated by the case of 3C321 which shows polarimetric evidence for a significant scattered quasar component, but also shows evidence for a starburst component in the form of a Balmer break and Balmer absorption features (Tadhunter et al. 1996, Robinson et al. 2000). It is notable that the starburst component in 3C321 only came to light through detailed modelling of the optical/UV continuum using a combination of spectrophotometry and spectropolarimetry measurements.

Given the complex circum-nuclear environments of powerful radio galaxies revealed by recent HST imaging studies (e.g. Jackson, Tadhunter & Sparks 1998), it is not surprising that no single mechanism is responsible for the UV excess. Observations of individual sources demonstrate the presence of at least four UV-emitting components that can contribute to the UV excess: scattered AGN light, direct AGN light, nebular continuum, and the light of young stellar populations. However, the relative importance of these components, and particularly the importance of any starburst component, is not clear from the previously published data. In this paper we attempt to remedy this situation by combining spectroscopic and polarimetric observations to quantify the contributions of the various UV-emitting components in a complete, optically unbiased sample of powerful 2Jy radio galaxies at intermediate redshifts ( $0.15 < z < 0.7$ ). We also consider the link between the optical/UV signs of star formation activity and the far-IR continuum excess. In a companion paper we report a similar study of a lower redshift sample of 3C radio galaxies ( $z < 0.2$ : Wills et al. 2002).

Throughout this paper we assume a Hubble constant of  $H_0 = 50 \text{ km s}^{-1} \text{ Mpc}^{-1}$  and a deceleration parameter of  $q_0 = 0$ .

## 2 SAMPLE SELECTION

The objects included in this study comprise radio galaxies selected from the Tadhunter et al. (1993) complete sample of 2Jy radio sources with redshifts  $z < 0.7$  and declinations  $\delta < +10$ , which is itself a subsample of the Wall and Peacock (1985) sample of radio sources with flux densities greater than 2Jy at 2.7 GHz. As discussed in Tadhunter et al. (1993, 1998) the  $z < 0.7$  sample has a high level of completeness. Low S/N optical spectra and identifications for all the  $z < 0.7$  sample are presented in Tadhunter et al. (1993) and di Serego Alighieri et al. (1994); radio maps for this sample are presented in Morganti et al. (1993, 1999); and X-ray observations are presented in Siebert et al. (1996). Discussion of the radio observations in the context of the unified schemes can be found in Morganti et al. (1995, 1997), while a discussion of the nature of the correlations between radio and optical emission line properties of the  $z < 0.7$  sample is presented in Tadhunter et al. (1998).

Although in section 4 below we will consider the UV excess in the  $z < 0.7$  sample of Tadhunter et al. 1993 as

Object	Other name	z	Radio Morph.	Optical Spect.
0023–26	OB-238	0.322	CSS	NLRG
0035–02	3C17	0.220	II	BLRG
0038+09	3C18	0.188	II	BLRG
0039–44		0.346	II	NLRG
0105–16	3C32	0.400	II	NLRG
0117–15	3C38	0.565	II	NLRG
0235–19	OD-159	0.620	II	(BLRG)
0252–71		0.566	CSS	NLRG
0347–05	4C05.16	0.339	II	BLRG
0409–75		0.693	II	NLRG
1306–09	OP-10	0.464	CSS	NLRG
1547–79		0.483	II	BLRG
1549–79		0.150	FSC	NLRG
1602+01	3C327.1	0.462	II	BLRG
1648+05	Her A	0.154	I/II	WLRG
1932–46		0.231	II	BLRG
1934–63		0.183	GPS	NLRG
1938–15		0.452	II	BLRG
2135–20	OX-158	0.635	CSS	(BLRG)
2211–17	3C444	0.153	II	WLRG
2250–41		0.310	II	NLRG
2314+03	3C459	0.220	II	NLRG

**Table 1.** Details of the sources in the complete sample of radio sources discussed in this paper. Column 4 gives the radio morphologies of the sample objects, based on the maps from Morganti et al. (1993), and Morganti et al. (1999) (key: II – Fanaroff Riley class II; I – Fanaroff Riley class I; CSS – compact steep spectrum ( $D < 15kpc$ ); FSC – flat spectrum core source; GPS – gigahertz peak spectrum radio source). The optical spectral classifications in column 5 are based on the deep spectra discussed in this paper and Tadhunter et al. (1998) (key: NLRG – narrow line radio galaxy; BLRG – broad line radio galaxy; WLRG – weak line radio galaxy). Objects for which the classification is uncertain are indicated by brackets.

a whole, most of this paper will be concerned with observations of a more restricted sample, selected to facilitate a more detailed study of the optical/UV continuum properties. The additional selection criteria for this restricted sample are: redshifts in the range  $0.15 < z < 0.7$  and right ascensions in the range  $13^h < RA < 05^h$ . The lower redshift limit for this restricted sample was chosen to ensure that the B-band filter used for the polarimetry observations covers the rest-frame UV for all the sample objects, while the RA restriction was intended to ensure that we observed a complete RA-limited sample of manageable size, given the constraints on the observing time. Some properties of the resulting sample of 22 objects are presented in Table 1.

The overall aim of our survey was to obtain accurate B-band polarimetry measurements and deep spectra covering at least the rest wavelength range  $3500 - 5500\text{\AA}$  for all of the restricted sample in Table 1. In reality, while we succeeded in obtaining deep spectra for the whole sample, time restrictions meant that we failed to obtain B-band polarimetry observations for three (15%) of the objects: the CSS source PKS0252-17, and the weak lined radio galaxies PKS1648+05 (Her A) and PKS2211-17(3C444). In the case of PKS0252-71 contamination by the light of a foreground galaxy precludes detailed study of the UV continuum prop-

Object	Date	S/W	PA (°)	Time (s)
0023–26	22/7/93	1.7/2	270	900(R + B)
0035–02	21/7/93	1.4/2	270	900(R) 600(B)
0038+09	22/10/95	1.7/5	270	900(B)
0039–44	23/7/93	1.5/2	270	900(R) 1200(B)
0105–16	23/7/93	1.5/2	270	900(B + R)
0117–15	23/7/93	1.5/2	270	900(B + R)
0235–19	20/10/95	1.5/5	270	2×900(B)
	20/10/95	1.5/5	270	600(B)
0252–71	21/7/94	1.5/5	270	600(B)
	21/7/94	1.5/5	270	900(R)
0347+05	22/10/95	1.5/5	270	600(B)
	22/10/95	1.5/5	270	300(R)
0409–75	22/10/95	1.4/2	208	700(B)
	22/10/95	1.4/2	208	600(R)
1306–09	23/7/93	1.3/2	270	900(R + B)
	12/7/94	1.8/2	270	900(R + B)
1547–79	20/7/93	1.2/2	270	900(R + B)
	22/7/93	1.3/2	270	900(B)
	23/7/93	1.2/2	270	900(B)
1549–79	12/7/94	1.9/5	270	1200(B)
1602+01	30/7/92	1.5/1.6	32	2×1200(R)
	30/7/92	1.5/2	32	1200(R)
1648+05	12/07/94	1.6/2	300	900(R + B)
1932–46	22/7/93	1.7/2	270	900(R + B)
	23/7/93	1.5/2	270	600(R + B)
1934–63	11/7/94	2.2/2	270	1200(B)
1938–15	22/7/93	1.3/2	211	900(R + B)
2135–20	23/7/93	1.5/2	270	1200(B)
	30/7/92	1.9/1.6	343	1200(R)
	30/7/92	1.9/2.0	343	3×1200(R + B)
2211–17	21/10/95	1.1/2	225	900(B)
2250–41	20/7/93	1.9/2	270	2×1200(B)
	20/7/93	1.9/2	270	900(R)
	22/7/93	1.6/2	270	1200(B)
2314+03	22/7/93	1.6/2	270	1200(B)
	22/7/93	1.6/2	270	600(R)

**Table 2.** Observational details of the spectroscopic observations for the objects in Table 1. Column 3 lists the seeing FWHM (S) and slit width (W) in arcseconds for the observations. Column 4 lists the position angle of the slit for each observation. Column 5 gives the integration time in seconds for each observation. All of the southern sample of radio galaxies were observed using EFOSC with the R300 and B300 gratings, with the exception of 1602+01 (3C327.1) which was observed with the red arm of the ISIS spectrograph on the 4.2m WHT telescope (30/7/92), and 2135-20, which was observed with the B300 grating of EFOSC (23/7/93 run) and with both the red and blue arms of ISIS on the WHT telescope.

erties, while for PKS1648+05 and PKS2211-17 it was felt that, considering of the lack of emission line activity, it was unlikely that any UV excess could be due to a polarized (scattered AGN) component. Failure to observe these three objects does not significantly affect our conclusions.

The key advantages of this survey for studying the UV excess are: (a) we have both polarimetric and spectroscopic observations for the overwhelming majority of the objects in Table 1, so our survey is not biased towards the brightest, most spectacular objects in the chosen redshift range; and (b) we have reduced the problem of varying dilution of any scattered component by the old stellar populations by observing all the objects in the rest-frame UV.

Some of the polarimetric and spectroscopic results from

the survey have already been published in Shaw et al. (1995) and Tadhunter et al. (1994). Here we present results for the remainder of the sample in Table 1, and discuss the results for this sample collectively.

### 3 OBSERVATIONS AND REDUCTIONS

B-band polarimetry data and long-slit spectra for most of the objects in Table 1 were obtained in three runs on the ESO 3.6m telescope at La Silla in Chile between 1993 and 1995. All the data from these runs were taken with the ESO Faint Object Spectrograph and Camera No.1 (EFOSC1) with a thinned TEK chip (No. 26), resulting in an angular scale of 0.62 arcseconds/pixel.

Long-slit spectra for the sample were obtained using the R300 and B300 grisms in EFOSC1 (see Melnick et al. 1989). These grisms together provide complete coverage of the observed wavelength range 3600 to 9900Å with a dispersion of 6.2Å/pixel for the B300 grism and 7.3Å/pixel for the R300 grism. The instrumental resolution was  $\sim 20\text{Å}$  with the 2 arcsecond slit. With this coverage it was possible to cover at least the rest wavelength range 3500-5500Å for all of the objects observed with EFOSC1. Details of the spectroscopic observations are given in Table 2.

In addition to the spectra obtained with EFOSC for most of the sources, two of the objects — 3C327.1 and PKS2135-20 — were observed using the 4.2m William Herschel Telescope (WHT) on La Palma with the ISIS dual-beam spectrograph. Both objects were observed using the R158R grating on the red arm of ISIS with an EEV CCD detector and a GG495 order sorting filter, yielding a dispersion of 2.72Å/pixel and a resolution of 10Å for a 1.6 arcsecond slit.

The B-band polarimetric observations were obtained with EFOSC1 in polarimetric mode with a Wollaston prism and aperture mask in the beam. For the 1993 and 1994 runs the polarized signal was modulated by using the Cassegrain instrument rotator to rotate the field relative to the Wollaston prism successively through a sequence of four rotator positions separated by 45 degrees. However, for the 1995 run the signal was modulated by using a half-wave plate in the beam, and rotating the half-wave plate through the sequence 0,22.5,45,67.5 degrees. Details of the polarimetric observations are given in Table 3.

#### 3.1 Spectroscopic reductions

The spectroscopic reductions followed the standard steps of bias subtraction, flat-fielding, wavelength calibration, atmospheric extinction correction, flux calibration and sky subtraction. The flux calibration was based on an average flux calibration curve derived from wide-slit observations of, typically, three flux calibration stars in each run. Comparisons between the flux calibration curves derived from individual standard star observations show that the relative flux calibration uncertainty is typically  $\pm 5\%$  over most of the wavelength range, but rises to  $\pm 10\%$  in the UV ( $\lambda < 4200\text{Å}$ ) and near-IR ( $\lambda > 8000\text{Å}$ ). By using a relatively wide slit, making the observations as close as possible to the zenith, and, in some cases, making observations with the slit aligned

Object	Date	S(")	Time(s)	$\lambda_W(\text{Å})$
0023-26	10/7/94	1.8	2×4×600	2780—4080
0035-02	20/10/95	1.7	4×600	3010—4420
	22/10/95	1.8	4×600	
0038+09	20/10/95	1.6	4×600	3090—4540
	22/10/95	1.6	4×600	
0039-44	10/7/94	1.8	2×4×300	2730—4000
0105-16	11/7/94	1.7	2×4×600	2620—3850
	21/10/95	1.7	4×900	
0117-15	20/10/95	1.5	4×900	2340—3440
	21/10/95	1.4	4×900	
0235-19	20/10/95	1.5	4×600	2270—3330
	21/10/95	1.2	4×600	
0252-71	—	—	—	—
0347+05	22/10/95	1.4	4×600	2740—4030
0409-75	22/10/95	1.4	4×600	2170—3180
1306-09	10/07/94	2.0	2×4×600	2500—3680
	11/07/94	1.8	2×4×600	
1547-79	20/7/93	1.2	4×900	2470—3630
	21/7/93	1.7	4×900	
1549-79	11/07/94	2.3	2×4×300	3190—4690
1602+01	21/07/93	1.8	2×4×900	2510—3690
1648+05	—	—	—	—
1932-46	10/7/94	2	2×4×600	2980—4380
1934-63	23/7/93	1.7	4×900	3100—4556
1938-15	10/7/94	2	2×4×600	2530—3710
	11/7/94	1.9	2×4×600	
2135-20	23/7/93	1.3	4×900	2245—3300
2211-17	—	—	—	—
2250-41	20/7/93	1.5	4×900	2800—4110
	21/7/93	1.4	4×900	
	23/7/93	1.5	4×900	
2314+03	20/10/95	1.7	4×300	3010—4420

**Table 3.** Observational details of the B-band polarimetric observations for the objects in Table 1. Column 3 lists the seeing FWHM for the observations. Column 4 lists the integration time for each complete cycle of four polarimetry measurements. Column 5 lists the approximate, rest frame, wavelength range sampled by the B-band filter.

along the parallactic angle, the effects of differential refraction were minimised. Only in two cases does differential refraction significantly affect the accuracy of the flux calibration: PKS1547-79 (airmass  $> 1.5$ ) and to a much lesser extent PKS2314+03 (airmass  $\sim 1.2$ ).

1 dimensional spectra of the near-nuclear regions were extracted from the 2 dimensional frames using extraction apertures that contained the bulk of the visible continuum emission (typically 2 – 4 arcseconds along the slit).

#### 3.2 Polarimetry

Following bias subtraction, cosmic ray removal, and correction for non-uniformities using flat-fields, the mean background level was determined for the ‘o’ and ‘e’-ray images separately, using several apertures placed evenly around the source. The ‘o’ and ‘e’-ray intensities for the radio galaxies were measured through circular apertures that included the bulk of the light in the near-nuclear regions (typically 3 – 6 arcseconds diameter) for each telescope rotator position or half-wave plate position, with the aperture size fixed through each cycle of rotator of four half-wave plate

Object	$P_{meas}$	$P_{int}$	$\theta_{opt}$ ( $^{\circ}$ )	$\theta_{radio}$ ( $^{\circ}$ )
0023–26	< 2.0	< 3.5	-	-
0035–02	$2.8 \pm 0.3$	$5.6 \pm 0.6$	$60 \pm 8$	$149 \pm 10$
0038+09	< 1.9	< 2.5	-	-
0039–44	$4.8 \pm 1.2$	$8.0 \pm 2.0$	$177 \pm 4$	$99 \pm 9$
0105–16	< 4.4	< 27	-	-
0117–15	$8.2 \pm 0.9$	$30.0 \pm 3.3$	-	-
0235–19	< 4.3	< 5.7	-	-
0252–71	-	-	-	-
0347+05	< 4.3	< 4.3	-	-
0409–75	< 6.3	< 6.3	-	-
1306–09	$6.3 \pm 1.3$	$8.4 \pm 1.7$	$110 \pm 5$	$137 \pm 4$
1547–79	$2.8 \pm 1.0$	$2.8 \pm 1.0$	-	-
1549–79	< 1.8	< 1.9	-	-
1602+01	< 4.5	< 7.5	-	-
1648+05	-	-	-	-
1932–46	< 1.6	< 3.7	-	-
1934–63	$3.5 \pm 0.5$	$8.5 \pm 1.2$	$8.0 \pm 3.5$	$90 \pm 1$
1938–15	< 5.5	< 8.9	-	-
2135–20	< 2.7	< 3.6	-	-
2211–17	-	-	-	-
2250–41	$4.9 \pm 0.7$	$18.6 \pm 2.7$	$152 \pm 5$	$97 \pm 2$
2314+03	< 1.2	< 1.3	-	-

**Table 4.** Summary of the results of the B-band polarimetry of the sample of southern radio galaxies corrected for positive bias (Simmons & Stewart 1985).  $P_{meas}$  is the measured polarization corrected for bias, while  $P_{int}$  is the intrinsic polarization corrected for contamination by unpolarized narrow line emission, old stellar populations and nebular continuum (see section 5.1 for details). The measured position angle of the polarization ( $\theta_{opt}$ ) is shown in Column 4 and, for comparison, the radio PA is included in Column 5. The polarization PA and radio PA for 0035–02 are taken from Tadhunter et al. (1992), the polarization and radio PAs for 1934–63 are from Tadhunter et al. (1994), and for 2250–41 the polarization and radio PAs are taken from Shaw et al. (1995).

positions. The intensities for all the rotator positions were then combined according to the prescription of Tinbergen and Rutten (1992) to produce the final polarization degrees and position angles shown in Table 4. The advantage of this technique for measuring the polarization is that, since it involves the ratios of the ‘o’ and ‘e’-ray intensities at each rotator/half-wave plate position, it is not sensitive to small photometric variations between the images. By combining the intensity ratios from rotator positions separated by 90 degrees, or half-wave plate positions separated by 45 degrees, any instrumental polarization produced in the instrument is automatically eliminated.

The uncertainties in the individual ‘o’- and ‘e’-ray intensities were estimated by combining the estimated uncertainty in the subtracted background (from the standard deviation in the background measurements), with the uncertainty due to the poissonian fluctuation in the source+background counts in the source aperture. These uncertainties were then propagated through the calculation of the polarization degree and angle. The final polarization measurements and upper limits shown in Table 4 have been corrected for the positive bias in the polarization following the prescription of Simmonds and Stewart (1985).

For the 1993 and 1994 runs, which used the telescope rotator to modulate the polarization, the polarization angles were calibrated using observations of polarization standard stars observed using the same techniques in the same runs. However, for the 1995 run, which used the half-wave plate, it was not possible to derive accurate polarization position angles because of problems with the initialisation of the half-wave plate at the end of each cycle; although the degrees of polarization measured for individual polarized sources and polarized standard stars were found to be consistent from one cycle to the next, large variations were found in the measured angles between the cycles. For the significantly polarized objects observed in this run, the values of the polarization listed in Table 4 represent the average of the polarization values measured independently for each of the two cycles of half-wave plate positions. In the case of objects without significant polarization but two cycles of observations from the 1995 run, the data were analysed independently for each cycle, and upper limits were derived from one cycle of observations only.

As a final check on the reliability of the measurements, the individual ‘o’ and ‘e’-ray intensity measurements for each cycle were checked to determine whether they followed the pattern expected for linearly polarized light. This allowed us to check for spurious polarizations which might arise, for example, from a cosmic ray affecting one of the images. The degrees of polarization measured for the polarized standard stars were found to be consistent with the published values, within the estimated uncertainties. Apart from PKS1934–63 (see Tadhunter et al. 1994), all the significant polarization measurements listed in Table 4 are based on two cycles of rotator/half-wave plate positions and have been checked for consistency between the cycles.

## 4 RESULTS

With the exception of section 4.1, which will include results from the full  $z < 0.7$  sample of Tadhunter et al. (1993), the results presented below are for the restricted sample ( $0.15 < z < 0.7$ ) listed in Table 1.

### 4.1 4000Å break measurements

Much of the early work on the continuum properties of radio galaxies concentrated on studies of their broad-band colours. Although this work provided evidence for blue or UV excesses in a large fraction of powerful radio galaxies compared with normal ellipticals, the approach of using the broad-band colours has the disadvantages that: (a) the broad-band filters may be contaminated in some redshift ranges by emission lines; and (b) the sensitivity of a particular broad-band colour to the UV excess depends on redshift. For example, the optical/near-IR broad-band colours are sensitive to UV excesses in high redshift ( $z > 0.5$ ) radio galaxies (e.g. Lilly & Longair 1984), but lose sensitivity for lower redshift objects.

An alternative way of quantifying the UV excess, which minimises these problems, is to use measurements of the 4000Å continuum break, which is prominent in the spectra of evolved stellar populations (D(4000): Bruzual 1983). However, some care is required when measuring the 4000Å break in powerful radio galaxies, since the bands used in

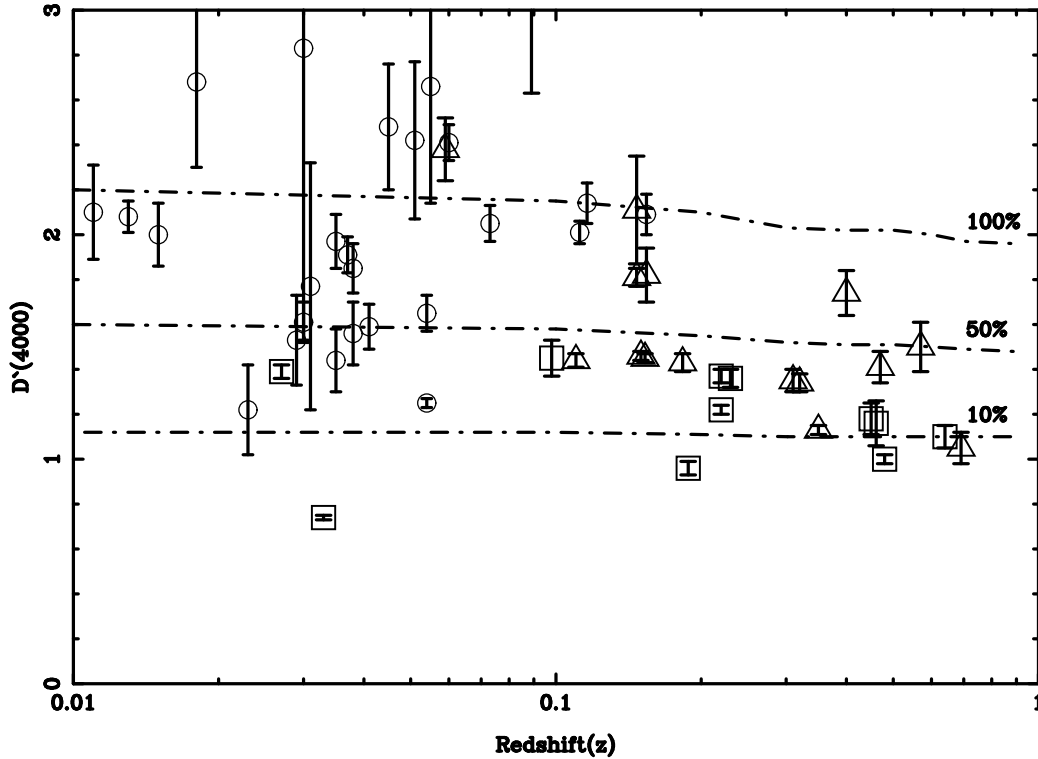


**Figure 1.** The parameter  $D'(4000)$  is sensitive to the presence of an excess UV flux compared to evolved stars below  $4000\text{\AA}$  in the rest frame of an object. Two separate datasets have been plotted here: the low redshift ( $z < 0.15$ ) radio galaxies with spectra published in Tadhunter et al. (1993); and the complete sample of  $0.15 < z < 0.7$  radio galaxies presented in Table 1. NLRG are shown as triangles, BLRG as squares, and WLRG as circles. The three solid curves represent the break of a passively evolving elliptical with a formation redshift,  $z_f=5$ . The models are from Bruzual & Charlot (1993) and are based on an instantaneous burst with Salpeter (1955) initial mass function. The three curves represent values of the break for which 100, 50 and 10% of the light below a rest frame wavelength of  $4000\text{\AA}$  is due to evolved stars.

the original definition of the  $D(4000)$  are contaminated by  $[\text{NeIII}]$ ,  $[\text{SII}]$  and  $\text{H}\delta$  emission lines, which can be strong in the spectra of radio galaxies. Therefore we use a modified version —  $D'(4000)$  — which is defined as the ratio of the total flux in a bin  $100\text{\AA}$  wide centred on  $4200\text{\AA}$  (rest frame) to the total flux in a  $100\text{\AA}$  wide bin centred on  $3800\text{\AA}$ . The narrower bands used in this definition avoid strong emission lines, although the contamination by the higher order Balmer lines may still be significant in some objects. The measurement of values of  $D'(4000)$  significantly lower than this indicates a UV excess. It is worth emphasising that an additional advantage of using  $D'(4000)$  to quantify the UV excess is that it is relatively insensitive to flux calibration errors and intrinsic reddening effects.

Measurements of  $D'(4000)$  for the restricted  $0.15 < z < 0.7$  sample in Table 1 are listed in Table 5 and plotted against redshift in Figure 1. For comparison purposes, values of  $D'(4000)$  for the remainder of the  $z < 0.7$  sample with spectra published in Tadhunter et al. (1993)\* — comprising lower redshift objects ( $z < 0.15$ ) — are also plotted in Fig-

ure 1. The measured values are compared with theoretical  $D'(4000)$  predictions for passively evolving elliptical galaxies, as derived from the models of Bruzual & Charlot (1993). The final column of Table 5 gives an estimate of the proportion of continuum light just below the  $4000\text{\AA}$  break that is contributed by continuum components other than an old stellar population. This has been calculated from  $D'(4000)$ , under the assumption that the additional continuum component has a flat spectrum.

There are several noteworthy features of these results:

- **Higher redshift objects.** All the objects at  $z > 0.15$  show evidence for a UV excess, with the old stellar populations contributing  $< 80\%$  of the flux at wavelengths shortward of  $4000\text{\AA}$ .
- **Lower redshift objects.** Although many lower redshift ( $z < 0.15$ ) radio galaxies have  $D'(4000)$  values consistent with a large fraction of light from an old stellar population, a significant proportion of objects ( $\sim 35\%$ ) show smaller values, suggesting a significant UV excess (see also Wills et al. 2002).
- **Weak line radio galaxies (WLRG).** Many of the lower redshift objects with evidence for a UV excess are

\* Note that the sample of low redshift objects with spectra published in Tadhunter et al. (1993) is biased against objects with strong emission lines (NLRG, BLRG). This is because many of the strong emission line sources had previously published spectra. Therefore they were not re-observed as part of the survey,

although they do, of course, form part of the overall  $z < 0.7$  complete sample of Tadhunter et al. (1993).

Object	D'(4000)	F <sub>D4000</sub>
0023—26	1.34 ± 0.04	0.63
0035—02	1.22 ± 0.02	0.80
0038+09	0.97 ± 0.03	1.00
0039—44	1.13 ± 0.02	0.87
0105—16	1.74 ± 0.02	0.28
0117—15	1.50 ± 0.11	0.50
0235—19	1.05 ± 0.15	0.95
0252—71	—	—
0347+05	1.13 ± 0.17	0.87
0409—75	1.05 ± 0.07	0.95
1306—09	1.41 ± 0.07	0.60
1547—79	1.00 ± 0.02	1.00
1549—79	1.46 ± 0.02	0.59
1602+01	1.16 ± 0.10	0.84
1648+05	1.82 ± 0.12	0.26
1932—46	1.36 ± 0.04	0.67
1934—63	1.43 ± 0.04	0.62
1938—15	1.18 ± 0.07	0.82
2135—20	1.10 ± 0.05	0.90
2211—17	1.54 ± 0.22	0.60
2250—41	1.35 ± 0.05	0.66
2314+03	1.37 ± 0.03	0.66

**Table 5.** Measurements of D'(4000) for the complete sample of 2Jy radio galaxies. The last column gives the estimated fraction of light in the wavelength range 3750 — 3950Å that is *not* associated with an old stellar population.

WLRG which do not show strong emission lines. This indicates that the presence of the UV excess is not always linked to the classic signs of AGN activity.

Before considering the continuum shapes in more detail it is important to emphasise that other factors than the UV excess can affect the 4000Å break. For example, a lower metallicity than assumed in the models can lead to lower values of D'(4000), because of the reduced effect of metal line blanketing in the atmospheres of the old stars at  $\lambda < 4000\text{\AA}$ . Although lower metallicity may be a factor in objects which have D'(4000) only marginally lower than the theoretical predictions in Figure 2, the metallicity would have to be unusually low in order to explain many of the values listed in Table 5.

## 4.2 UV polarization measurements

From the results of polarimetry measurements presented in Table 4, it is clear that high UV polarization is rare in our sample of intermediate redshift radio galaxies. Only 7 out of 19 (37%) of the objects in Table 1 with UV polarization measurements are significantly polarized in the UV; only 4 have measured polarization at the  $P_B > 5\%$  level; and none is highly polarized at the  $P_B > 10\%$  level. For the majority of the sources it has only been possible to derive upper limits on the polarization.

It is notable that, of the significantly polarized sources, the two with the lowest UV polarization — PKS0035-02 and PKS1547-79 — are both broad line radio galaxies (BLRG), and in the case of PKS1547-79 it is possible that much of the UV polarization is due to dichroic extinction by dust in our Galaxy (Shaw et al. 1995). None of the remaining 7

BLRG in our sample is significantly polarized in the UV, despite the substantial UV excesses measured in all of these objects. Therefore the incidence of objects with high UV polarization in the population of BLRG appears relatively low. In contrast, most of the objects with significant UV polarization are NLRG, and the incidence of significant UV polarization amongst the NLRG is higher: 5 out of 10 (50%) of the NLRG with good polarization measurements show significant UV polarization.

The last two columns in Table 4 give the optical polarization (E-vector) and radio axis position angles, for the few cases for which it has been possible to measure the PAs accurately. In most cases, the polarization angle is either close to the perpendicular to the radio axis (PKS0035-02, PKS0039-44, PKS1934-63) or the perpendicular to the UV structure axis (PKS2250-41: Shaw et al. 1995), in line with measurements of other powerful radio galaxies (e.g. Cimatti et al. 1993). The only major exception is PKS1306-09, for which the polarization angle is closer to the parallel to the radio axis. This suggests that the polarization mechanism in PKS1306-09 may be different from that in the other sources.

## 4.3 Nebular continuum

The nebular continuum, which comprises a combination of 2-photon, free-free, and free-bound continuum, as well as a pseudo continuum due to blended higher order Balmer lines (see Dickson et al. 1995), is the best-constrained of the components which may contribute to the UV excess. This is because it scales directly with the  $H\beta$  flux and is relatively insensitive to the physical conditions, ionization and metallicity. The only major uncertainty with this component is the line of sight reddening, which will act to reduce the flux of the observed nebular continuum at UV wavelengths relative to the  $H\beta$  flux.

Prior to the more detailed continuum modelling described in section 4.4, the nebular continuum spectrum was calculated from the measured  $H\beta$  flux for each object using the STARLINK DIPSO package. The spectrum of the pseudo continuum due to blended higher order Balmer lines was also generated (see Dickson et al. 1995) and added to the DIPSO output. The calculation of the nebular continuum was made for an electron temperature of 15,000 K and a density of  $100\text{ cm}^{-3}$ .

The estimated fractional contribution of the nebular continuum to the observed UV continuum of all the objects in Table 1 with good  $H\beta$  and UV continuum flux estimates is shown in Table 6. These estimates were made for a 100Å continuum bin centred just below the Balmer continuum recombination break — where the nebular continuum has its peak flux. Since no account has been taken of reddening, these estimates represent an upper limit on the true fractional contribution of the nebular component to the UV continuum. The effect of the reddening of the nebular continuum on the continuum modelling will be discussed in section 4.4 below.

It is clear from Table 6 that the nebular continuum makes a significant contribution to the UV continuum in all of the sample objects, comprising 3 — 40% of the continuum below the Balmer break.

Nebular fraction	
0023—26	0.37±0.04
0035—02	0.11±0.02
0038+09	0.05±0.01
0039—44	0.19±0.02
0105—16	0.12±0.02
0117—15	0.29±0.06
0235—19	0.11±0.02
0252—71	—
0347+05	—
0409—75	0.12±0.04
1306—09	0.10±0.01
1547—79	—
1549—79	0.14±0.02
1602+01	0.17±0.08
1648+05	0.11±0.03
1932—46	0.18±0.02
1934—63	0.15±0.03
1938—15	0.15±0.02
2135—20	0.14±0.02
2211—17	0.05±0.01
2250—41	0.27±0.02
2314+03	0.03±0.01

**Table 6.** The fractional contribution of the nebular continuum to the UV flux. The ratios have been calculated from the mean fluxes in a 100Å bin centred on 3590Å (rest-frame), for both the observed nuclear spectra and the theoretical nebular spectra. In each case the nebular spectrum was calculated from the H $\beta$  flux assuming an electron density of 100cm<sup>-3</sup> and a temperature of 15000 K and zero reddening.

#### 4.4 Modelling

In order to gain further information about the nature of the UV continuum we have attempted to model the continuum spectral energy distributions (SEDs) in terms of various spectral components which may, potentially, contribute to the UV excess. Prior to this modelling effort we subtracted the nebular continuum calculated as described in section 4.3, and assuming no reddening in this component.

Given that radio galaxies have early-type continuum morphologies at optical wavelengths, we started by assuming that the nebular-subtracted optical-UV continuum SEDs comprise a combination of an old stellar population and a power-law. For the old stellar population we used the instantaneous burst model of Bruzual and Charlot (1983), for a Salpeter IMF and age (since the starburst) of 15Gyr. The power-law was used to represent the “active” component e.g. scattered AGN light or direct AGN light, with the power-law spectral index allowed to vary over the range  $-6 < \alpha < +6$  ( $F_{\lambda} \propto \lambda^{+\alpha}$ ).

As a first step to modelling the spectra, continuum fluxes were measured in a number of wavelength bins, chosen to avoid strong emission lines, cosmetic defects and regions of poor sky subtraction or poor flux calibration. Errors for the continuum flux measurements were calculated by quadratically combining the Poisson noise in sky+object signal, an assumed relative flux calibration error of  $\pm 5\%$ , and an estimate of the systematic error in the background subtraction, determined by examining spatial slices covering the wavelength range of each bin, as extracted from the

Object	$\chi^2$	$\alpha$	$F_{model}$
0023—26	2.07	3.3	0.55
0035—02	0.94	0.1 <sup>+0.6</sup> <sub>-1.4</sub>	0.60 <sup>+0.16</sup> <sub>-0.14</sub>
0038+09	1.20	0.1 <sup>+0.4</sup> <sub>-1.8</sub>	0.91 <sup>+0.09</sup> <sub>-0.45</sub>
0039—44	1.04	0.1 <sup>+0.6</sup> <sub>-1.0</sub>	0.70 <sup>+0.12</sup> <sub>-0.16</sub>
0105—16	0.69	2.7 <sup>+4.2</sup> <sub>-3.8</sub>	0.25 <sup>+0.36</sup> <sub>-0.24</sub>
0117—15	0.95	-0.5 <sup>+2.4</sup> <sub>-6.8</sub>	0.24 <sup>+0.23</sup> <sub>-0.16</sub>
0235—19	0.71	-1.5 <sup>+1.2</sup> <sub>-1.0</sub>	0.67 <sup>+0.10</sup> <sub>-0.08</sub>
0347+05	3.10	-0.9	0.88
0409—75	4.30	1.7	0.91
1306—09	0.26	1.1 <sup>+0.8</sup> <sub>-2.6</sub>	0.64 <sup>+0.23</sup> <sub>-0.24</sub>
1549—79	2.52	1.7	0.45
1602+01	1.15	-0.5 <sup>+1.4</sup> <sub>-1.4</sub>	0.69 <sup>+0.24</sup> <sub>-0.23</sub>
1648+05	1.42	1.7 <sup>+1.4</sup> <sub>-0.8</sub>	0.24 <sup>+0.17</sup> <sub>-0.05</sub>
1932—46	1.41	0.7 <sup>+0.8</sup> <sub>-1.8</sub>	0.62 <sup>+0.16</sup> <sub>-0.14</sub>
1934—63	1.01	-0.1 <sup>+1.8</sup> <sub>-1.8</sub>	0.45 <sup>+0.30</sup> <sub>-0.23</sub>
1938—15	0.66	0.9 <sup>+0.8</sup> <sub>-1.8</sub>	0.70 <sup>+0.17</sup> <sub>-0.32</sub>
2135—20	2.01	-0.1	0.82
2211—17	0.59	0.3 <sup>+1.4</sup> <sub>-2.2</sub>	0.54 <sup>+0.30</sup> <sub>-0.23</sub>
2250—41	0.69	0.9 <sup>+0.6</sup> <sub>-2.8</sub>	0.55 <sup>+0.35</sup> <sub>-0.22</sub>
2314+03	3.96	-0.3	0.82

**Table 7.** Results of modelling the SED’s of the southern sample of radio galaxies using two-component — 15 Gyr galaxy plus power law — models. Column 2 is the reduced  $\chi^2$ . Column 3 is the spectral index of the power-law ( $f_{\lambda} \propto \lambda^{\alpha}$ ). Column 4 lists the fraction of the total model continuum flux (including the nebular component) contributed by the fitted power-law component in a wavelength bin just shortward of the 4000Å break (3750 — 3850Å). Where no confidence interval is quoted the probability of the best-fit model was less than 5%.

sky-subtracted 2D spectra. The fluxes and errors were estimated in 15 – 30 bins for each object (depending on the useful wavelength range for each spectrum), and the fitting was then performed using the minimum  $\chi^2$  technique detailed in Tadhunter et al. (1996).

The results of the modelling are shown in Table 7 and Figure 2. Only objects with significant fits are shown in the Figure. In most objects the power-law+E-galaxy model provides an adequate fit to the data, with the power-law component contributing 20 — 90% of the continuum just below the 4000Å break (see final column in Table 7). This confirms the results based on the 4000Å break measurements described in section 4.1. Note, however, that the proportional contribution of the power-law to the UV continuum at wavelengths just below 4000Å is systematically less than estimates derived from D’(4000) (compare the last columns of Tables 5 and 7). This difference is likely to be due to the fact that the D’(4000) measurements were made before the subtraction of the nebular continuum, and therefore overestimate the contributions of the putative power-law components. No modelling was performed for PKS1547-79 because of the effects of differential atmospheric refraction on the flux measurements. Also, poor sky subtraction, weak signal and relatively short exposure times are likely to be responsible for the relatively poor fits obtained for PKS0409-75 and PKS0347+05.

One interesting general feature of the results in Table 7 is that, in the majority of cases, the fitted power-law spec-

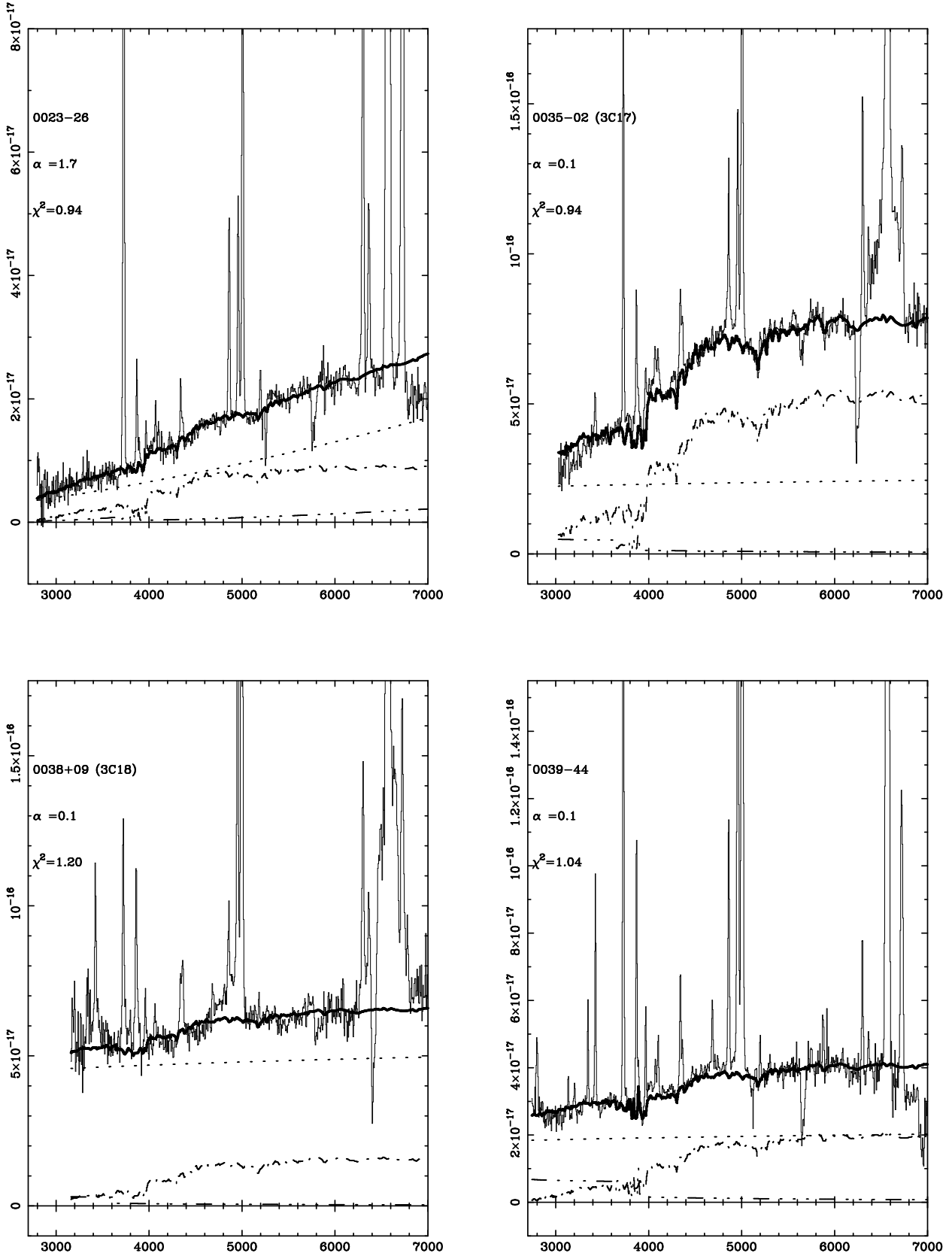


**Figure 2.** Power-law plus 15Gyr elliptical galaxy fits to the continua of the complete sample of radio galaxies. The best-fit model continuum spectrum is indicated by the thick continuous line. The 15Gyr elliptical galaxy component is indicated by a dot-dash line, the power-law component by a dotted line and the nebular continuum by a dot-dot-dot-dash line. The fluxes are in units of  $\text{ergs cm}^{-2} \text{s}^{-1} \text{Å}^{-1}$ .

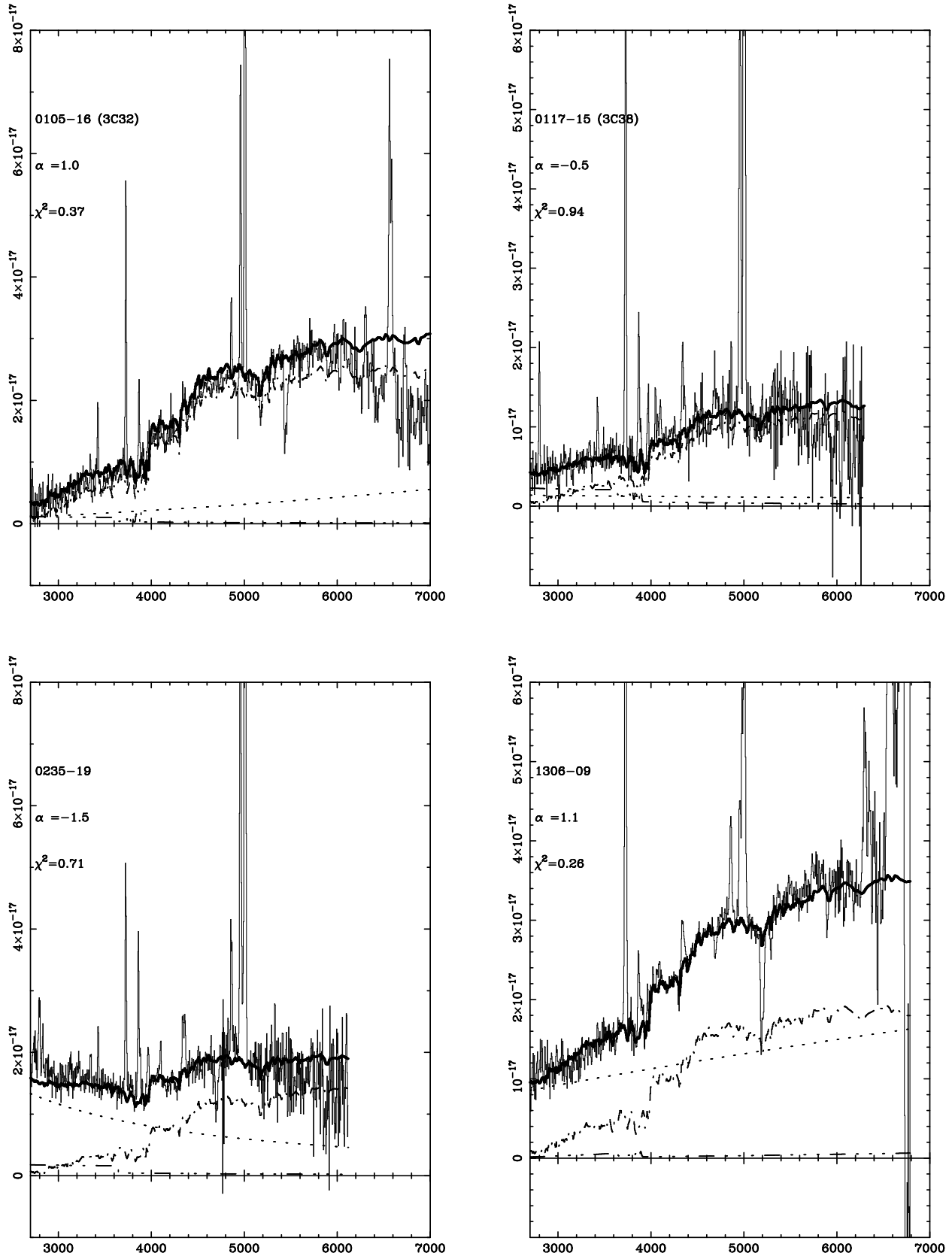


Figure 2. Cont.

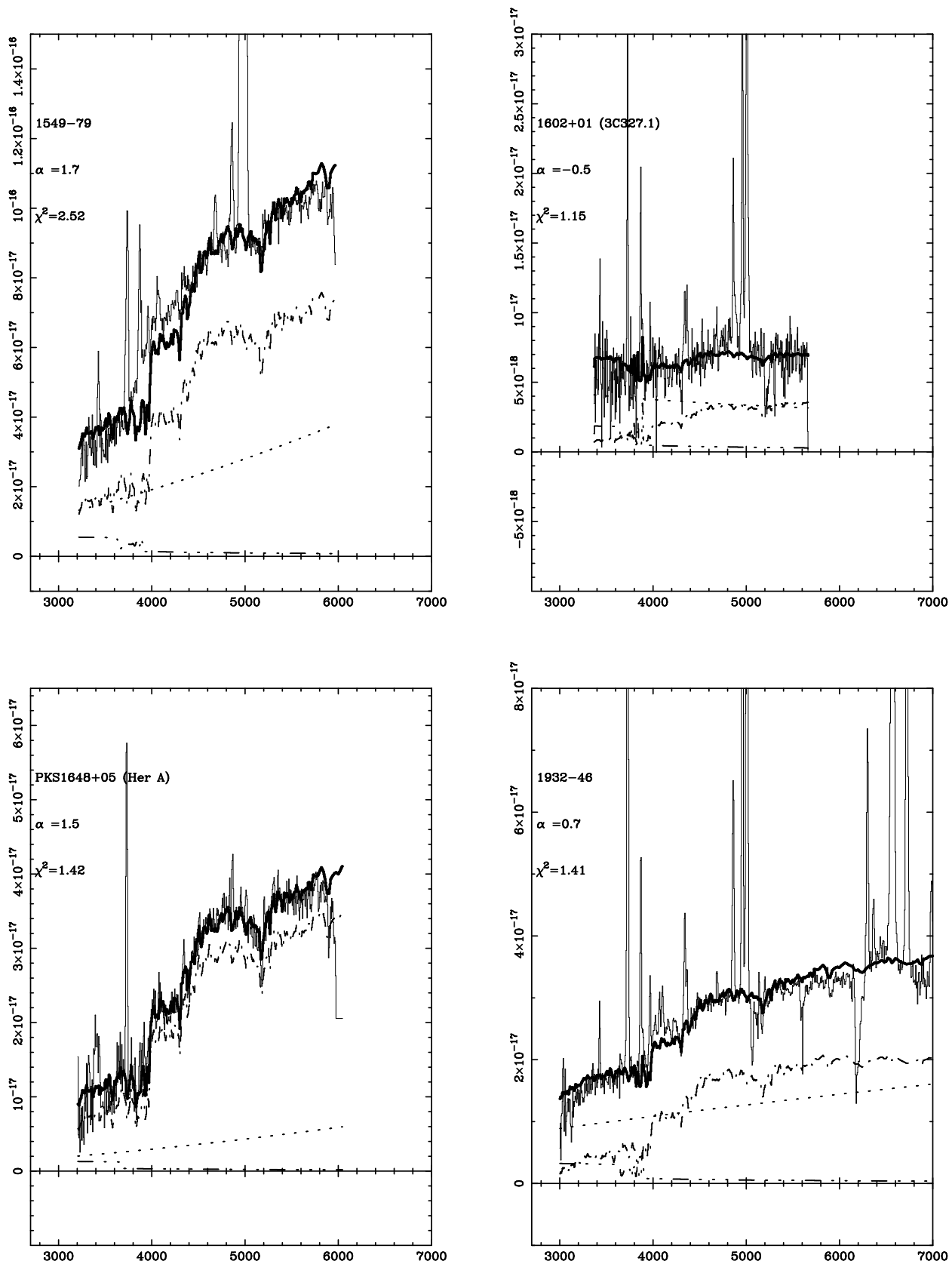


Figure 2. Cont.

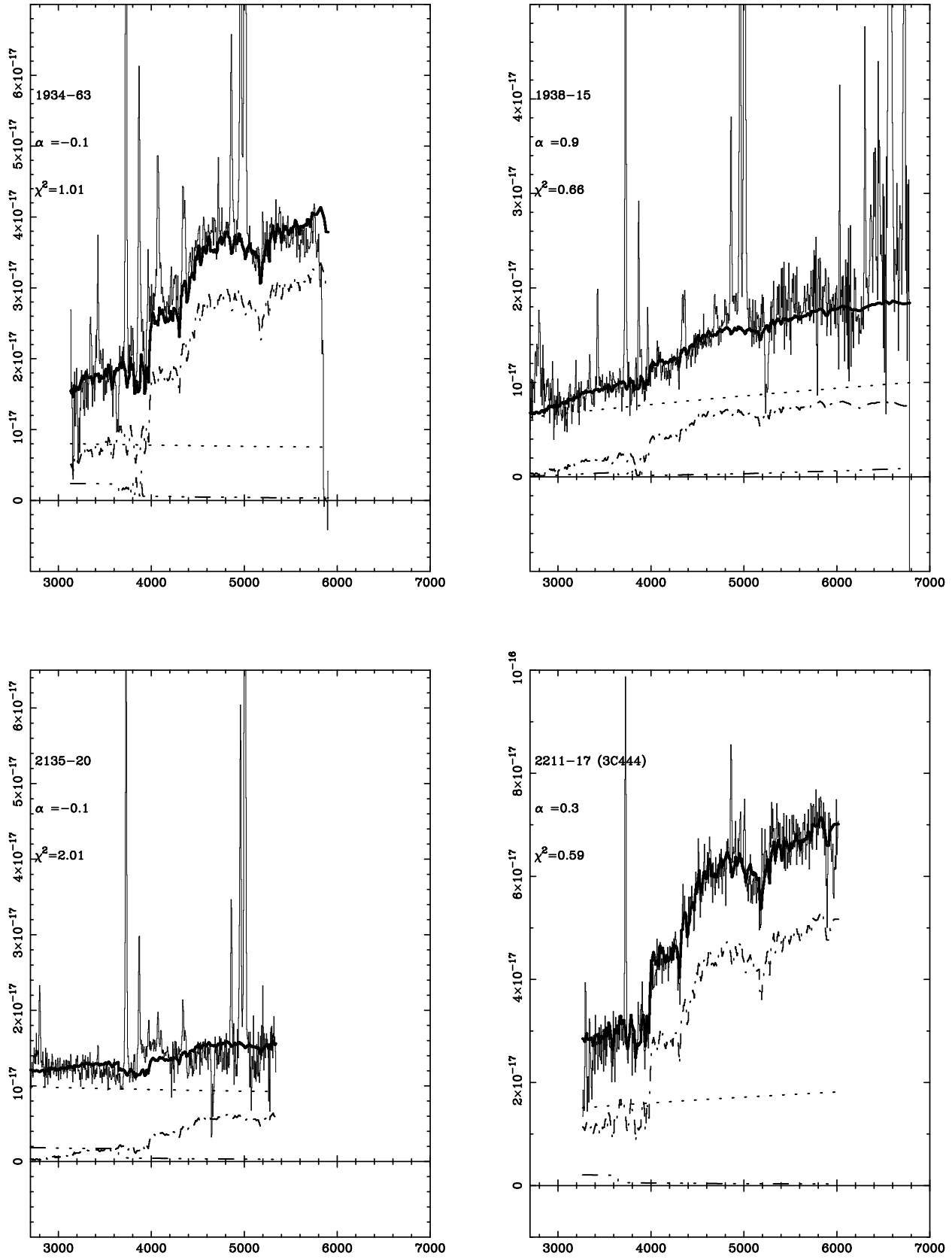


Figure 2. Cont.

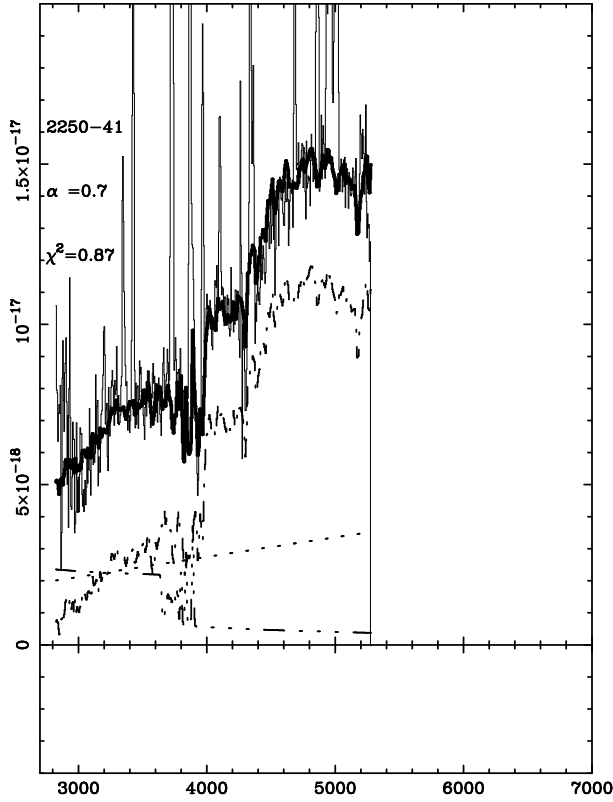


Figure 2. Cont.

tral indices are redder than the mean  $\alpha = -1.3$  derived for the optical/UV continua of quasars by Christiani & Vio (1990) over the range 1000 – 5500 Å. They are also redder than most  $z < 0.7$  quasars in the southern 2Jy sample of Tadhunter et al. (1993), which have measured optical (3000 – 5500 Å) spectral slopes in the range  $-2.8 < \alpha < -0.5$ ; and high redshift quasars in the sample of Kuhn et al. (2001) which have UV-optical slopes in the range  $-2.2 < \alpha < -0.8$ . Therefore, if the power-law component represents direct or scattered AGN light, then it is likely that this component is significantly reddened in many of the objects.

Given that the results of the modelling are potentially sensitive to the effects of reddening on the subtracted nebular continuum<sup>†</sup>, we repeated the modelling following subtraction of a nebular continuum reddened by the amount determined from the emission line Balmer decrement assuming case B recombination theory, for cases in which the reddening was deemed significant. The results are shown in Table 8. Subtraction of the reddened nebular continuum leads to significantly improved fits in the case of PKS0023-26 and PKS1648+05, but in most other cases the improvement is marginal. As expected, given that less nebular continuum is being subtracted from the UV excess, the proportional contribution of the power-law component is larger in these models, and the power-law slope is bluer.

<sup>†</sup> Note that the effects of reddening on the power-law component will be reflected in the fitted spectral index for that component. We assume in our modelling that the 15Gyr old stellar population is not significantly affected by reddening.

Object	$\chi^2$	$\alpha$	$F_{model}$	E(B-V)
0023-26	0.94	$1.7^{+0.2}_{-1.0}$	$0.66^{+0.18}_{-0.28}$	1.18
0105-16	0.37	$1.9^{+4.2}_{-3.8}$	$0.24^{+0.35}_{-0.23}$	1.10
1306-09	0.12	$0.7^{+2.6}_{-1.0}$	$0.67^{+0.27}_{-0.27}$	0.80
1549-79	1.59	$1.5^{+0.2}_{-0.8}$	$0.58^{+0.08}_{-0.16}$	0.61
1648+05	0.95	$1.5^{+1.0}_{-4.4}$	$0.27^{+0.11}_{-0.06}$	0.94
1938-15	0.86	$0.5^{+0.8}_{-2.4}$	$0.75^{+0.21}_{-0.29}$	0.95

**Table 8.** Results of modelling the SEDs of the southern sample of radio galaxies using two-component — 15 Gyr galaxy plus power law — models including reddening of the nebular continuum. The columns are the same as Table 7 except column 5, which gives the degree of reddening estimated from the Balmer decrement.

However, for three objects — PKS1549-79, PKS2135-20, PKS2314+03 (3C459) — we failed to obtain good fits to the nebular continuum subtracted SEDs using two component E-galaxy+power-law models, despite the good quality of the data. In all of these cases we found a significant excess of the data over the models in the wavelength range 3750 – 4300 Å. In addition, higher order Balmer absorption lines are detected in all three objects either in our own spectra or published spectra (see di Serego Alighieri et al. 1997 for a higher resolution spectrum of PKS1549-79), and both PKS2135-20 and PKS2314+03 have relatively blue continuum slopes at wavelengths larger than 4500 Å. All of these features are consistent with a significant contribution from young stellar populations (see Tadhunter et al. 1996, Robinson et al. 2000). Therefore we have attempted to model the continua of the three objects with various combinations of old and young stellar populations (using the instantaneous burst models of Bruzual & Charlot 1993) and power-laws. We have also tried models in which the young stellar populations were reddened by varying degrees. The best fitting models are shown in Table 9, and compared with the data in Figure 3. In the case of PKS1549-79 and PKS2135-20 we obtained an adequate fit using models which combine an old (15Gyr) and young stellar populations (reddened in the case of PKS1549-79). On the other hand, in the case of PKS2314+03 the best fit comprised a combination of young stellar populations with two starburst ages plus a power-law. Given that the spectrum of PKS2135-20 has a relatively low S/N, that of PKS1549-79 has a relatively small spectral coverage, and that of PKS2314+03 may be affected by differential atmospheric refraction effects (see section 3.1), the modelling estimates of the ages of the young stellar populations should not be regarded definitive. Nonetheless, these results provide strong evidence that the optical/UV continua of all three objects are dominated by the light of young stellar populations with ages in the range 0.1 – 2Gyr.

#### 4.5 Notes on individual objects

**PKS0023-26.** This CSS radio galaxy has a large UV excess, but a low polarization, and no sign of broad permitted lines in its spectrum. A possible starburst candidate.

**PKS0035-02 (3C17).** The strength of the broad permitted lines in this BLRG suggests that much of its UV excess is due to direct AGN light. However, given the significant

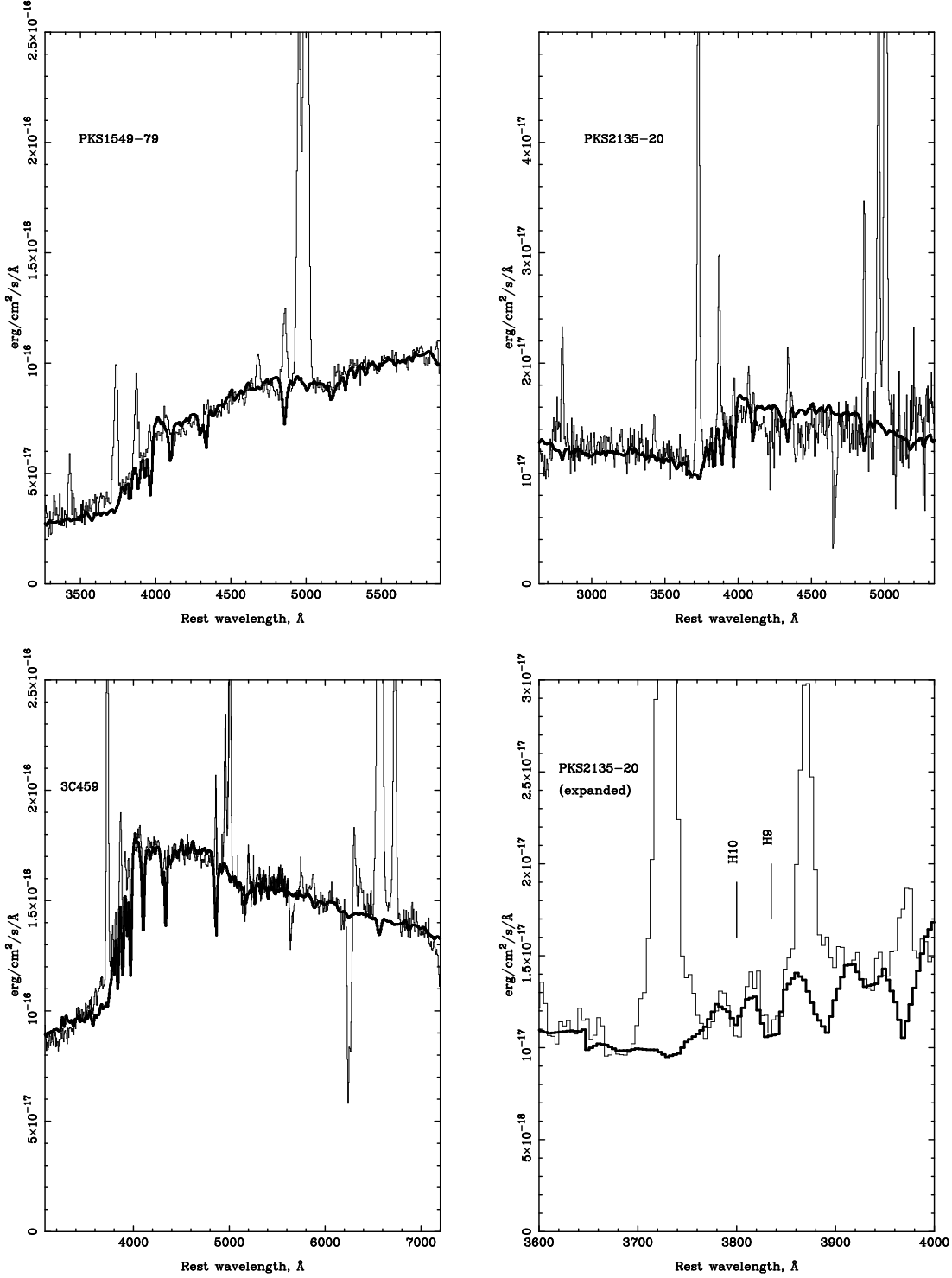


**Figure 3.** Fits to the continua of PKS1549–79, PKS2135–20 and PKS2314+03(3C459) that include young stellar populations. While two-component elliptical galaxy plus power-law or quasar models cannot reproduce the continuum SEDs of PKS1549–79, PKS2135–20 and PKS2314+03(3C459), models in which the spectra are dominated by young stars are successful. PKS1549–79 has been modelled by the spectrum of an 1 Gyr population reddened by  $E(B-V)=0.4$  while PKS2135–20 is shown plotted with a model comprising an unreddened 0.1 Gyr population, and PKS2314+03 (3C459) has been modelled with a combination of a 1Gyr starburst, a 0.5Gyr starburst and a power-law (see Table 9). The lower right hand panel shows an expanded plot of the region around the Balmer break in PKS2135–20 with the higher Balmer lines (H9,H10) labelled. In all cases the best fitting continuum models are indicated by thick solid lines.

Object	$\chi^2$	Age	$F_{ys}$	$F_{pl}$	E(B-V)
PKS1547-79	0.56	1.0	0.88	—	0.4
PKS2135-20	0.74	0.1	0.90	—	0.0
PKS2314+03	0.29	1.0,0.5	0.34,0.28	0.36	0.0
	0.51	2.0,0.1	0.64,0.38	—	0.0,0.2

**Table 9.** Best fitting models for PKS1549-79, PKS2135-20 and PKS2314+03 that include young stellar populations, yield formally significant fits, and reproduce the excess flux seen in the wavelength interval 3900Å–4300Å over the two component (power-law+E-galaxy fits) models. In the case of PKS2314+03 the fitting results are shown for models both with and without a power-law component. The third column gives the age in Gyr for the best-fitting young stellar populations, while the fourth and fifth columns give the fractional contributions of the young stellar populations and power-law to the total flux in the normalising bin respectively.

polarization detected at both UV wavelengths (this paper) and optical wavelengths (Tadhunter et al. 1992), scattered AGN light may also contribute. Optical synchrotron emission is a plausible alternative to scattered AGN light in this source, given the distorted S-shaped radio structure, and relatively strong core-jet visible in high resolution radio maps (Morganti et al. 1999).

**PKS0038+09 (3C18).** Direct AGN light is likely to contribute much of the UV excess in this BLRG which has a low UV polarization.

**PKS0039-44.** This FR II radio galaxy has a large UV excess, significant UV polarization, but no broad permitted lines. Although the scattered AGN light is likely to be significant, given the relatively low level of intrinsic polarization (Table 4), it is unlikely that this component dominates the UV continuum. A possible starburst candidate.

**PKS0105-44 (3C32).** This FR II radio galaxy has a modest UV excess, no significant UV polarization, and no clear detection of broad permitted lines. The origin of its UV excess is not clear.

**PKS0117-15 (3C38).** This high redshift FR II radio galaxy is one of the most highly polarized objects in our sample. Given the high intrinsic polarization (Table 4), it is likely that scattered AGN light dominates the UV excess in this source.

**PKS0235-19.** This FR II radio galaxy shows a large UV excess, but has a low UV polarization. Weak broad wings are marginally detected to the H $\beta$  and MgII(2800) permitted lines, but deeper spectroscopic observations are required to confirm that this is a BLRG in which the UV excess is dominated by direct AGN light.

**PKS0252-71.** Contamination of images and spectra by a foreground galaxy preclude detailed study of the optical continuum in this CSS radio galaxy.

**PKS0347-05.** This unusual FR II radio galaxy has broad permitted lines but only weak narrow lines (di Serego Alighieri et al. 1994). Although it has not been possible to model the continuum of this object in detail because of a

poor sky subtraction, given the low level of UV polarization, it is likely that direct AGN light contributes much of its UV excess.

**PKS0409-75.** This FR II radio galaxy is the highest redshift source in our sample. This object clearly has a large UV excess, but it has not been possible to model its continuum in any detail because of a poor sky subtraction. The relatively low UV polarization and failure to detect broad permitted lines make this a strong starburst candidate.

**PKS1306-09.** This CSS radio galaxy has a large UV excess, only narrow emission lines, and significant UV polarization. Given that the polarization E-vector angle is closer to the parallel than the perpendicular to the radio axis, the polarization mechanism may not be anisotropic scattering, but some alternative mechanism such as dichroic absorption or synchrotron emission. The low level of intrinsic polarization suggests that, in the case that the polarization mechanism is anisotropic scattering, the scattered component does not dominate the UV excess.

**PKS1547-79.** This BLRG is one of the most luminous sources in our sample. Its continuum properties have been extensively discussed in Shaw et al. (1995), who argue that at least some of the significant UV polarization measured in this source may be due to dichroic absorption in our Galaxy. Differential diffraction effects preclude detailed modelling of its continuum, but it is likely that the UV excess in this object is dominated by direct AGN light.

**PKS1549-79.** The narrow emission line properties of this extraordinary flat spectrum radio galaxy have been discussed in detail by Tadhunter et al. (2001). It is likely that this is an intrinsically compact radio source in which the radio jets are pointing close to our line of sight, but the quasar nucleus is entirely extinguished by dust on a kpc-scale. No broad permitted lines are detected in our optical spectra of this source, and we detect no significant UV polarization in our observations. However, di Serego Alighieri et al. (1997) report significant optical polarization at the  $\sim 3\%$  level in both the optical continuum and [OIII] emission lines in their smaller aperture observations. This polarization could have either a scattering or a dichroic origin, however, it is unlikely that the polarized component dominates the UV excess. Both our continuum modelling, and the detection of Balmer lines in absorption in the higher resolution observation of di Serego Alighieri et al. (1997) are consistent with a starburst dominating the optical/UV continuum in this source.

**PKS1602+01 (3C327.1).** This FR II radio galaxy has been discussed in detail by Shaw et al. (1995), who classify it as a BLRG on the basis of the clear detection of broad H $\beta$  emission lines. Given the failure to detect significant UV polarization it is likely that the UV excess in this source is entirely dominated by direct AGN light.

**PKS1648+05.** This powerful radio source, with a morphology between FRI and FR II, has weak narrow emission lines in its optical spectrum, and the smallest UV excess of any source in Table 1. The continuum measurements presented in this paper refer to the brighter of the two nuclei visible in

optical images of the core region. The cause of the apparent UV excess is unknown.

**PKS1932-46.** Villar-Martin et al. (1998) report the detection of a broad H $\alpha$  emission line in this FRII radio galaxy (also visible in the spectrum in Figure 2), but it shows no significant UV polarization. The residuals from the two component continuum model fit suggest a significant contribution from a starburst component, in addition to direct AGN light. The spectacular extended emission line nebulosity surrounding the galaxy is described in detail by Villar-Martin et al. (1998).

**PKS1934-63.** As discussed in Tadhunter et al. (1994), this GPS radio galaxy is significantly polarized in the UV with the polarization E-vector close to perpendicular to the radio axis. No broad permitted lines are detected in our optical spectra. It is likely that scattered AGN light makes a significant contribution to the UV excess in this source.

**PKS1938-15.** This FRII shows broad H $\beta$  and MgII(2800) emission lines in its optical/UV spectrum, but is not significantly polarized in the UV. Therefore its UV excess is likely to be dominated by direct AGN light.

**PKS2135-20.** Shaw et al. (1995) have reported the detection of broad MgII(2800) in this CSS radio galaxy. However, its classification as a BLRG is not certain because of the possibility that blended narrow high ionization lines make a contribution to the broad wings of MgII(2800) in our low resolution spectrum (e.g. Dey & Spinrad 1996, Tran et al. 1998). The detection of the Balmer break higher Balmer absorption lines (H9, H10: see Figure 3) in our optical spectrum suggests a dominant contribution from a starburst component, and this is confirmed by our continuum modelling. PKS2135-20 may be a radio-loud example of the “post-starburst quasar” phenomenon first reported by Brotherton et al. (1999).

**PKS2211-17.** Despite the fact that it belongs to the class of weak line radio galaxies, with no broad permitted lines detected in its optical spectrum, this FRII radio galaxy displays a substantial UV excess. A significant contribution from a starburst component is suspected.

**PKS2250-41.** The continuum properties of this FRII radio galaxy have been discussed in detail by Shaw et al. (1995) and Dickson et al. (1995). Its optical spectrum shows only narrow emission lines, but it is significantly polarized in the UV with the polarization E-vector close to the perpendicular to the UV structural axis. The relatively high intrinsic polarization suggests that scattered AGN light makes a substantial contribution to the UV excess in the nuclear regions. Clark et al. (1997) and Villar-Martin et al. (1999) describe detailed spectroscopic and imaging observations of a spectacular jet-cloud interaction on the west side of the nucleus.

**PKS2314+05 (3C459).** The optical/UV spectrum of this FRII radio galaxy is clearly dominated by the light of a young stellar population, with the Balmer break and higher Balmer absorption lines clearly detected (see also Miller 1981). Our spectrum shows no clear evidence for broad permitted lines.

## 5 DISCUSSION

### 5.1 The scattered AGN component

Our polarization measurements of a complete, optically unbiased sample allow us to gauge for the first time the significance of the scattered AGN component in UV continua of the general population of powerful radio galaxies.

We detect significant UV polarization in only a relatively small fraction ( $\sim 37\%$ ) of our sample, and the level of polarization is relatively low in the objects that are polarized ( $P_B < 10\%$ ). Moreover, scattering of the anisotropic quasar light is not the only polarization mechanism, but other mechanisms such as dichroic absorption and synchrotron radiation may also contribute. Therefore it is safe to conclude that the scattered AGN component does not dominate the UV light in the majority of sources in our sample. For pure scattered light we would expect to measure polarization at the  $P > 10\%$  level, even allowing for the geometrical dilution caused by integrating over the broad radiation cones of the illuminating AGN (Young et al. 1995, Manzini & di Serego Alighieri 1996).

By assuming that all the polarization is due entirely to the power-law component (see section 4.4), we can use the fractional contribution of the power-law in the B-band filter, as determined from our modelling, to estimate the intrinsic polarization of the polarized component. In this way we automatically correct for the contributions of the old stellar populations and the nebular continuum, which are assumed to be unpolarized. A further assumption implicit in this procedure is that the fractional contribution of the polarized component is the same in the (different) apertures used for the spectroscopic and polarimetric observations, which is not necessarily the case. The results, which have also been corrected for emission line contamination in the filter band-pass, are shown in Table 4. From this it can be seen that the high levels of intrinsic polarization estimated for PKS2250-41 and PKS0117-15(3C38) are consistent with scattered light comprising a large fraction of the power-law component. However, in most of the other cases, the relatively low levels of intrinsic polarization ( $P_{int}$ ) suggest that other, unpolarized, sources of UV light may contribute to the component modelled as a power-law.

Figure 4 shows the intrinsic polarization plotted as a function of redshift. Although the upper envelope defined by the three most highly polarized sources shows evidence for a rise in the intrinsic polarization with redshift, taking the sample as a whole, and including the upper limits, this trend does not appear to be significant.

The proportion of highly polarized sources in our sample is somewhat less than found in other studies (Tadhunter et al. 1992, Cimatti et al. 1993, Vernet et al. 2001). Possible reasons for this include the following.

- **Observational biases of previous studies.** Because the polarization measurements are difficult to make, previous surveys are likely to have been biased towards the most spectacular and luminous radio galaxies in a given redshift range. Moreover, null results may not be always be reported in the literature.
- **Selection frequency of the current survey.** The selection frequency of the 2Jy sample (2.7GHz) is higher than for most other samples. However, it is not clear that

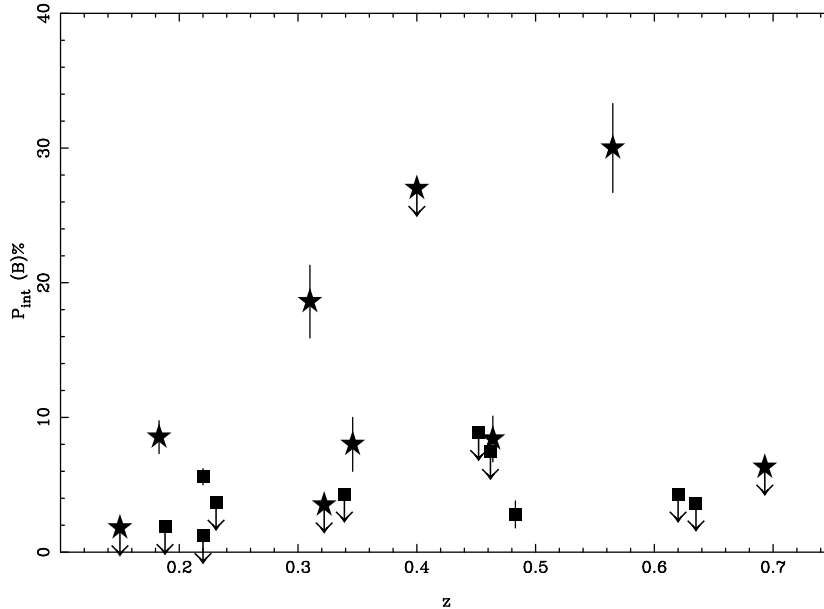


**Figure 4.** Plot of the intrinsic polarization as a function of redshift for the sample in Table 1. The BLRG are indicated by filled squares, and the NLRG are indicated by filled stars.

this will necessarily bias our sample against high UV polarization. Most of our sources would in any case have been selected in low frequency surveys.

- **Redshift dependent effects.** For a given density of scatterers the strength of the scattered component will depend on the luminosity of the central illuminating source. The radio power is strongly correlated with the redshift in flux limited samples such as the 2Jy sample. Also, since optical emission line luminosity is strongly correlated with radio power (e.g. Rawlings & Saunders 1991, Tadhunter et al. 1998), it is likely that the illuminating quasars hidden in the cores of the radio galaxies will become more luminous as the redshift increases. Therefore, we might expect the scattered quasar component to become more significant as the redshift increases and the sources become more powerful. Part of the difference between the results of our survey and those of previous surveys of higher redshift objects may be due to this effect.

The only way to unambiguously distinguish between these possibilities would be to make an optically unbiased survey of a large sample of radio galaxies selected from low frequency radio surveys at a single frequency, and spanning a wide range in redshift. However, if the last possibility is correct we would expect the most highly polarized sources in our sample to be those with the strongest signs of quasar activity, as deduced from the narrow emission line luminosities. Figure 5 shows a plot of [OIII] emission line luminosity against radio power for the sample in Table 1, with the significantly polarized objects highlighted. As discussed in Tadhunter et al. (1998), [OIII] is more sensitive to quasar ionizing luminosity than lower ionization emission lines such as [OII](3727) and  $H\beta$ , and it is likely that the large scatter in this plot is a consequence of a large range in the quasar luminosity for a given radio power. It is clear that many of the highly polarized sources fall close to the upper en-

velope of the [OIII] luminosity in this plot, thus suggesting that the objects with the most luminous quasars are also those with the greatest proportional contribution of scattered AGN light in the UV.

## 5.2 Direct AGN light

We have identified 9 objects in our sample ( $\sim 40\%$  of the total) which show broad permitted emission lines in their spectra and should therefore be classified as BLRG<sup>†</sup>. With the exception of PKS0035-02 (3C17), and possibly also PKS1547-79, none of the BLRG in our sample is highly polarized in the UV, despite the presence of large UV excesses. Therefore, it is likely that we are observing the nuclei directly in these sources, and that the UV excess is due to direct AGN light, with only a minor contribution, if any, from scattered AGN light. This is in line with polarimetric observations of low redshift BLRG and quasars which show low levels of polarization in most objects (Stockman, Angel & Miley 1979, Antonucci 1984). Clearly, objects such as 3C234 (Tran, Cohen & Goodrich 1995) and 3C109 (Goodrich & Cohen 1992), in which the broad lines are readily detected in optical spectra, and which also show a high degree of linear polarization, are the exception rather than the rule.

It is interesting to consider how these BLRG fit into the orientation-based unified schemes for powerful radio galaxies, in which it is proposed that radio galaxies and quasars are the same thing viewed from different directions, with the

<sup>†</sup> It is important to distinguish between these BLRG — in which the broad lines are readily visible in the straight intensity spectra — and objects in which the broad lines are only visible in polarized spectra or following detailed continuum modelling and subtraction (e.g. Cohen et al. 1999).

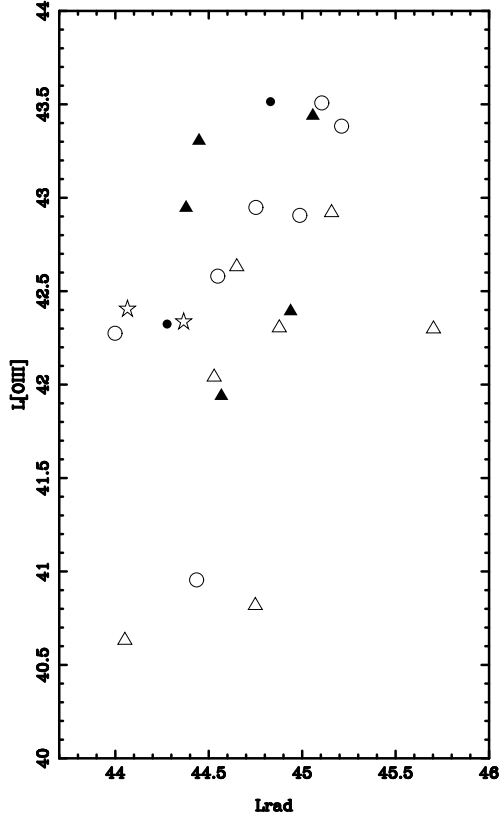


**Figure 5.** [OIII] emission line luminosity plotted against total radio power for the complete sample in Table 1. NLRG are indicated by triangles, while BLRG are indicated by circles. Filled symbols indicate objects for which a significant UV polarization has been detected. Stars indicate the two objects in our sample (PKS1549-79 & PKS2314+03) that are unusually bright at far-IR wavelengths.

quasar nucleus blocked from direct view in the radio galaxies by a central obscuring torus (Barthel 1989). There are two main possibilities:

- **They are partially obscured quasars.** In this case, the quasar nuclei would be observed at intermediate angles, such that they suffer mild extinction from the outer layers of the torus or the kpc-scale dust lane.
- **They are low luminosity quasars.** In this case, there would be a wide range of quasar luminosity at a given radio power — as already suggested by the large scatter in the correlation between [OIII] emission line luminosity and radio power (Tadhunter et al. 1998) — and the BLRG would represent the low luminosity end of the quasar luminosity function.

It would be difficult to distinguish between these possibilities based on the current data alone, but the relatively red slopes of the power-laws fitted to the BLRG in the two component model fits (see section 4.4) are more consistent with the first of these two possibilities. The partial obscuration idea is also consistent with the recent spectroscopic studies of quasars which suggest that a significant proportion of quasars are significantly reddened (e.g. Baker 1997) at optical wavelengths. Moreover, analyses of the radio properties

of the 2Jy sample, in particular the ratio of core to extended radio power, are consistent with the idea that the BLRG are observed with the radio axis at an intermediate angle to the line of sight (Morganti et al. 1997).

### 5.3 Young stellar populations

One of the most striking results from our survey is the emergence of a group of three radio galaxies (15% of the total) in which the optical/UV continua are dominated by the light of young stellar populations. Interestingly, these three radio galaxies — 3C459, PKS1549-79, PKS2135-20 — all have relatively compact radio sources: 3C459 has an extended double radio source on a scale of 48 kpc (Morganti et al. 1999), but also has a steep spectrum radio core, which is itself double; PKS2135-20 is classified as a compact steep spectrum radio source; and, although PKS1549-79 has a flat radio spectrum and a one sided jet structure extending to radial distances of 500pc, we have argued elsewhere on the basis of its emission line kinematics that this is an intrinsically compact radio source (Tadhunter et al. 2001).

It is relatively easy to detect the young stellar populations in PKS2135-20, PKS1549-79 and 3C459 because their optical continua are dominated by the young stars, and the ages of the starbursts (0.1 — 2Gyr) are such that the spectral features of the young stellar population are relatively easy to detect. However, it is possible that significant young stellar populations are present in other radio galaxies in our sample, but are more difficult to detect because the stellar populations are younger and/or are less luminous relative to the old stellar populations. In particular, there are three sources in our sample with large UV excesses — PKS0023-26, PKS0409-75, PKS2211-17 — for which we have failed to identify the cause of the UV excess, because they show neither significant UV polarization nor broad permitted lines, and the nebular continuum makes a relatively minor contribution to their UV emission. There are a further three objects — PKS0039-44, PKS1934-63, PKS1306-09 — which are significantly polarized in the UV, but the level of intrinsic polarization, if attributed solely to the power-law component, is less than expected for pure scattered light. Finally, we note that the residuals of the two component fits to the continuum of the weak broad line object PKS1932-46 — with a significant excess in the 3800 – 4300Å region and a blue continuum slope at longer wavelengths — are consistent with the presence of a young stellar population. Although young stellar populations may make a significant contribution in all of these objects, the relatively red slopes of the fitted power-laws for most of them (Tables 7 & 8) suggest that the starburst component must be significantly reddened.

Taking these six less certain cases along with three objects in which the young stellar populations dominate, we derive a conservative upper limit of 50% on the proportion of objects in our sample which have their optical/UV continua dominated by the light of young stellar populations. This is entirely consistent with the results from two recent surveys of lower redshift 3C radio sources in which ~30 – 40% of the objects show evidence for recent star formation activity (Aretxaga et al. 2001, Wills et al. 2001).

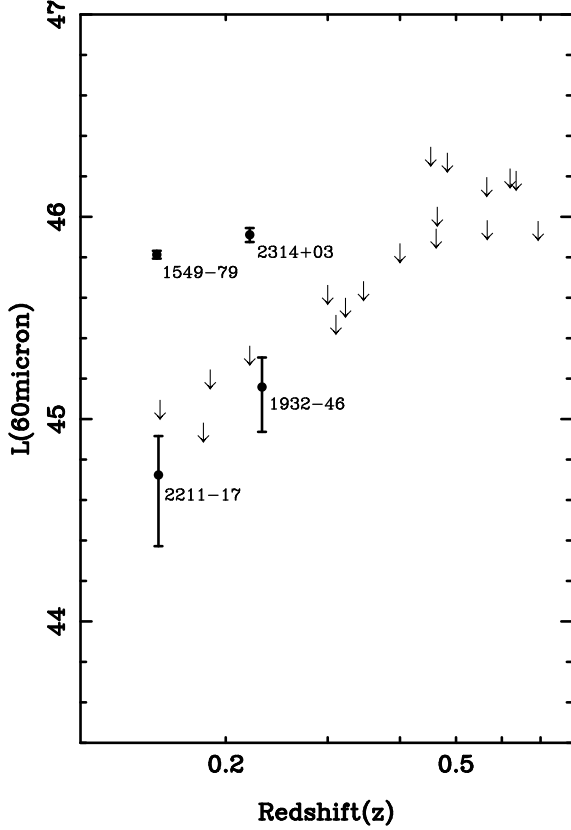


**Figure 6.** A plot of far-infrared ( $60\mu\text{m}$ ) luminosity against redshift.

#### 5.4 The far-IR/starburst link in powerful radio galaxies

The far-IR/sub-mm continuum excesses detected in some radio galaxies are often attributed to dust heated by starbursts (e.g. Rowan-Robinson 1995, Archibald et al. 2001). However, this interpretation is controversial, given the likely presence of powerful quasar nuclei hidden in the cores of the galaxies which could also heat the cooler dust component (Sanders et al. 1989). Indeed, the issues surrounding the nature of the far-IR continuum are similar to those surrounding the UV excess considered in this paper: is the far-IR/sub-mm excess primarily a direct consequence of the quasar activity, or is it a consequence of starbursts related to the evolutionary events that triggered the activity?

In order to investigate the links between the far-IR excess and optical/UV starburst activity, we have extracted  $60\mu\text{m}$  fluxes and  $3\sigma$  upper limits from IRAS ‘all-sky’ survey data. To do this we used the SCANPI algorithm available at IPAC to co-add individual IRAS scans. The IRAS co-added scans were then visually inspected in order to assess the significance of individual detections. The detection of an object was only considered significant if the positional offset in the detection was less than 0.5 arcminutes from the nominal position of the object, and the object was detected in more than one IRAS band. In cases without clear detections we quote  $3\sigma$  upper limits, where  $\sigma$  was taken as the RMS deviation from the baseline-corrected scans at  $60\mu\text{m}$ . The resulting fluxes and upper limits are presented in Table

Object	$F_{60\mu\text{m}}$ (Jy)	$\nu P_{60\mu\text{m}}$ ( $\text{erg s}^{-1}$ )
0023–26	$< 0.117$	$< 3.6 \times 10^{45}$
0035–02	$< 0.159$	$< 2.0 \times 10^{45}$
0038+09	$< 0.171$	$< 1.5 \times 10^{45}$
0039–44	$< 0.120$	$< 4.3 \times 10^{45}$
0105–16	$< 0.132$	$< 6.5 \times 10^{45}$
0117–15	$< 0.123$	$< 1.4 \times 10^{46}$
0235–19	$< 0.108$	$< 1.6 \times 10^{46}$
0252–71	$< 0.075$	$< 8.6 \times 10^{45}$
0347+05	$< 0.159$	$< 4.0 \times 10^{45}$
0409–75	$< 0.045$	$< 8.6 \times 10^{45}$
1306–09	$< 0.141$	$< 9.9 \times 10^{45}$
1547–79	$< 0.237$	$< 1.8 \times 10^{46}$
1549–79	$1.120 \pm 0.05$	$(6.5 \pm 0.3) \times 10^{45}$
1602+01	$< 0.111$	$< 7.9 \times 10^{45}$
1648+05	$< 0.186$	$< 1.1 \times 10^{45}$
1932–46	$0.100 \pm 0.04$	$(1.4 \pm 0.6) \times 10^{45}$
1934–63	$< 0.099$	$< 8.6 \times 10^{44}$
1938–15	$< 0.297$	$< 2.0 \times 10^{46}$
2135–20	$< 0.099$	$< 1.5 \times 10^{46}$
2211–17	$0.090 \pm 0.05$	$(5.4 \pm 1.9) \times 10^{44}$
2250–41	$< 0.105$	$< 2.9 \times 10^{45}$
2314+03	$0.630 \pm 0.05$	$(8.1 \pm 0.7) \times 10^{45}$

**Table 10.** Far-infrared ( $60\mu\text{m}$ ) fluxes and luminosities for the sample in Table 1, as derived from co-added IRAS scans. The  $\nu P_{60\mu\text{m}}$  luminosities were derived by assuming a far-IR continuum spectral index of  $\beta = -1.0$  ( $F_\nu \propto \nu^\beta$ ) over the wavelength range  $25 - 100\mu\text{m}$ .

10. We have also determined the  $60\mu\text{m}$  luminosities ( $\nu P_\nu$ ), by assuming a far-IR spectral slope of -1 (see Golombek et al. 1988). The luminosities are presented in the last column of Table 10, and plotted against redshift in Figure 6. It is notable that only 4 out of 22 of the sources in our sample were detected by IRAS at  $60\mu\text{m}$  with any certainty.

The most striking feature of the far-IR luminosities in Table 10 and Figure 6 is that two of the three objects in our sample dominated by optical/UV starbursts – PKS1549-79 & PKS2314+03 (3C459) – also stand out as being unusually luminous at far-IR wavelengths. Indeed, PKS1549-79 & PKS2314+03 (3C459) are the most far-IR luminous of the 12 objects in our sample at  $z < 0.40$ ; they are approximately a factor 5 –  $10\times$  brighter at far-IR wavelengths than the other 2Jy radio galaxies at similar redshifts. The third object dominated by an optical/UV starburst – PKS2135-20 – is at much higher redshifts and its  $60\mu\text{m}$  upper limit is consistent with it having a far-IR luminosity similar to those of PKS1549-79 & PKS2314+03. Note the [OIII] emission line luminosities of PKS1549-79 & PKS2314+03 are typical of radio galaxies at similar redshifts; they are not in any way extreme (see Figure 5). Therefore it is unlikely that the far-IR excesses result from heating of the cool dust by unusually luminous quasars, or that the covering factor of gas and dust is unusually large in these objects.

PKS1932-46 & PKS2211-17 were also marginally detected by IRAS. Again, these are both sources in which significant young stellar populations are suspected, based on their optical/UV spectra (see section 5.3).

Overall, despite the low rate of detection of the radio galaxies in our sample at far-IR wavelengths, there appears to be a link between the detection of optical/UV starburst

activity and the level of the far-IR excess. Recently, we obtained a similar result for a sample of lower redshift 3C sources (Wills et al. 2001): the object with the largest contribution from an optical/UV starburst in that sample (3C433) also has the largest far-IR luminosity. All of these results support the idea that the cooler dust components detected in radio galaxies are heated by starbursts rather than hidden quasar nuclei. The putative link between far-IR excess and optical/UV starburst activity for powerful radio galaxies will be discussed in more detail in a future paper (Tadhunter et al. 2002, in preparation).

### 5.5 Implications for studies of quasar host galaxies

If the unified schemes for powerful radio galaxies are correct, then radio galaxies *are* quasar host galaxies in which the quasar nuclei are hidden from our direct view. Therefore, we expect to find the same components contributing to the UV excess in the quasar hosts as we do in the powerful radio galaxies. Indeed, if the scattering dust grains are large relative to the wavelength of the optical/UV light, the scattered AGN component may be more significant in the quasar hosts, because of the forward scattering properties of the dust grains. On the basis the results reported above, it would be unwise to base any investigation of quasar host galaxy properties on continuum colours alone. Clearly, detailed spectroscopic and polarimetric observations are as important for disentangling the various components contributing to the optical/UV continuum in quasar hosts, as they are in powerful radio galaxies.

## 6 CONCLUSIONS AND FURTHER WORK

The results of our survey confirm the multi-component nature of the UV continuum in powerful radio galaxies. We can quantify the contributions of the various components that contribute to the UV excess in the near-nuclear regions as follows:

- **Nebular continuum.** This is present in the spectra of all the objects and contributes 5 – 40% of the UV continuum below the Balmer break.
- **Direct AGN light.** Based on the detection of broad permitted lines in the intensity spectra, direct AGN light makes a significant contribution to the UV excess in ~30 – 40% of the objects in our sample.
- **Scattered AGN light.** Polarimetric observations provide evidence that scattered AGN light makes a significant contribution to the UV continuum in 37% of the 19 objects in our sample with polarization measurements, but in most cases the scattered component does not appear to dominate the UV excess.
- **Starburst component.** Young stellar populations clearly dominate the optical/UV continua in three of the objects in our sample (~15%) and may make a large contribution to the optical/UV continuum in up to 50% of all the sample objects.

Of these components, the starburst component clearly warrants further investigation. If, as seems likely, the starbursts were triggered by the same merger events that trig-

gered the radio jet and quasar activity, then detailed studies of the starbursts can provide potentially unique information about the genesis of powerful radio sources, particularly the timescales, the nature of the mergers and the order-of-events.

### Acknowledgments

Based on observations collected at the European Southern Observatory, La Silla, Chile, and at the Roque de los Muchachos Observatory, La Palma. RD,MVM,TGR & KAW acknowledge support from PPARC while this work was being carried out.

## REFERENCES

- Antonucci, R.R.J., 1984, 278, 499  
 Archibald, E.N., Dunlop, J.S., Hughes, D.H., Rawlings, S., Eales, S.A., Ivison, R.J., 2001, MNRAS, 323, 417  
 Arctaxaga, I., Terlevich, E., Terlevich, R.J., Cotter, G., Diaz, A.I., 2001, MNRAS, 325, 636  
 Baker, J.C., 1997, MNRAS, 286, 23  
 Barthel, P.D., 1989, ApJ, 336, 606  
 Brotherton, M.S., van Breugel, W., Stanford, S.A., Smith, R.J., Boyle, B.J., Miller, L., Shanks, T., Croom, S.M., Filippenko, A.V., 1999, ApJ, 520, L87  
 Bruzual, A.G., 1983, ApJ, 273, 105  
 Bruzual, A.G., Charlot, S., 1993, ApJ, 405, 538  
 Christiani, S., Vio, R., 1990, A&A, 227, 385  
 Cimatti A., di Serego Alighieri S., Fosbury R., Salvati M., Taylor D., 1993, MNRAS, 264, 421  
 Clark, N.E., Tadhunter, C.N., Morganti, R., Killeen, N.E.B., Fosbury, R.A.E., Hook, R.N., Siebert, J., Shaw, M.A., 1997, MNRAS, 286, 558  
 Cohen, M.H., Ogle, P.M., Tran, H.D., Goodrich, R.W., Miller, J.S., 1999, AJ, 118, 1963  
 Dey, A., Spinrad, H., 1996, ApJ, 459, 133  
 Dickson, R., Tadhunter, C., Shaw, M., Clark, N. & Morganti, R., 1995, MNRAS, 273, L29  
 di Serego-Alighieri, S., Danziger, I.J., Morganti, R., Tadhunter, C.N., 1994, MNRAS, 269, 998  
 di Serego Alighieri, S., Cimatti, A., Fosbury, R.A.E., Hes, R., 1997, A&A, 328, 510  
 Fabian, A.C., 1989, MNRAS, 238, 41p  
 Golombek, D., Miley, G., Neugebauer, G., 1988, AJ, 95, 26  
 Goodrich, R.W., Cohen, M.H., 1992, ApJ, 391, 623  
 Heckman T.M., Smith E.P., Baum S.A., van Breugel W.J.M., Miley G.K., 1986, 311, 526  
 Heckman, T.M., O'Dea, C.P., Baum, S.A., Laurikainen, E., 1994, ApJ, 428, 65  
 Jackson, N., Tadhunter, C.N., Sparks, W., 1998, MNRAS, 301, 131  
 Kuhn, O., Elvis, M., Bechtold, J., Elston, R., 2001, ApJS in press (astro-ph/0105255)  
 Lilly, S.J., Longair, M.S., 1984, MNRAS, 211, 833  
 Manzini, A., di Serego Alighieri, S., 1996, A&A, 311, 79  
 Melnick, J., Dekker, H., D'Odorico, S., 1989, ESO Operating Manual No.4 – ESFOSC  
 Melnick, J., Gopal-Krishna, Terlevich, R., 1997, A&A, 318, 337  
 Miller, J.S., 1981, PASP, 93, 681  
 Morganti, R., Killeen, N.E.B., Tadhunter, C.N., 1993, MNRAS, 263, 1023  
 Morganti, R., Oosterloo, T.A., Fosbury, R.A.E., Tadhunter, C.N., 1995, MNRAS, 274, 393

- Morganti, R., Oosterloo, T.A., Reynolds, J.E., Tadhunter, C.N., Migenes, V., 1997, *MNRAS*, 284, 541
- Morganti, R., Oosterloo, T., Tadhunter, C.N., Aiudi, R., Jones, P., Villar-Martin, M., 1999, *A&AS*, 140, 355
- Ogle, P.M., Cohen, M.H., Miller, J.S., Fosbury, R.A.E., Goodrich, R.W., 1997, *ApJ*, 482, 370
- Rawlings, S., Saunders, R., 1991, *Nat*, 349, 138
- Robinson T. G., Tadhunter C. N., Axon D. J., Robinson A., 2000, *MNRAS*, 317, 922
- Rowan-Robinson M., 1995, *MNRAS*, 272, 737
- Salpeter E. E., 1955, *ApJ*, 121, 161
- Sanders D. B., Phinney E. S., Neugebauer G., Soifer B.T., Matthews K., 1989, *ApJ*, 347, 29
- Siebert, J., Brinkmann, W., Morganti, R., Tadhunter, C.N., Danziger, I.J., Fosbury, R.A.E., di Serego Alighieri, S., 1996, *MNRAS*, 279, 1331
- Simmons J., Stewart B., 1985, *A&A*, 142, 100
- Shaw M., Tadhunter C., Dickson R., Morganti R., 1995, *MNRAS*, 275, 703
- Smith, E.P., Heckman, T.M., 1989, *ApJ*, 341, 658
- Stockman, H., Angel, J., Miley, G., 1979, *ApJ*, 227, L55
- Tadhunter C., Fosbury, R.A.E., di Serego Alighieri S., 1988, in Maraschi L., Maccacaro T., Ulrich M.-H., eds, *Proc. Como Conf. 1988, BL Lac Objects*. Springer-Verlag, Berlin, p.79
- Tadhunter, C., Scarrott S., Draper P., Rolph C., 1992, *MNRAS*, 256, 53p
- Tadhunter C., Morganti R., di Serego Alighieri S., Fosbury R., Danziger I., 1993, *MNRAS*, 263, 999
- Tadhunter, C., Shaw, M.A., Morganti, R., 1994, *MNRAS*, 271, 807
- Tadhunter, C.N., Dickson, R.C., Shaw, M.A., 1996, *MNRAS*, 281, 591
- Tadhunter, C.N., Dickson, R., Morganti, R., Villar-Martin, M., 1997, *Proceedings of the ESO Workshop on Quasar Hosts*, Clements, D & Perez-Fornoun, I. (eds), Springer-Verlag, p311
- Tadhunter, C.N., Morganti, R., Robinson, A., Dickson, R., Villar-Martin, M., Fosbury, R.A.E., 1998, *MNRAS*, 297, 936
- Tadhunter, C., Wills, K., Morganti, R., Oosterloo, T., Dickson, R., 2001, *MNRAS* in press (astro-ph/0105146)
- Tinbergen, J., Rutten, R., 1992, *ING User Manual*, XXI
- Tran, H.D., Cohen, M.H., Goodrich, R.W., 1995, *AJ*, 110, 2597
- Tran, H.D., Cohen, M.H., Ogle, P.M., Goodrich, R.W., di Serego Alighieri, S., 1998, *ApJ*, 500, 660
- Vernet, J., Fosbury, R.A.E., Villar-Martin, M., Cohen, M.H., Cimatti, A., di Serego Alighieri, S., Goodrich, R.W., 2001, *A&A*, 366, 7
- Wall, J., Peacock, J., 1985, *MNRAS*, 216, 173
- Villar-Martin, M., Tadhunter, C., Clark, N., 1998, *A&A*, 323, 21
- Villar-Martin, M., Tadhunter, C., Morganti, R., Axon, D., Koeckmoer, A., 1999, *MNRAS*, 307, 24
- Wills, K.A., Tadhunter, C.N., Robinson, T.G., Morganti, R., 2002, *MNRAS* submitted
- Young, S., Hough, J.H., Axon, D.J., Bailey, J.A., Ward, M.J., 1995, *MNRAS*, 272, 513